

Synchrotron intensity plots from a relativistic stratified jet

V. A. Frolova^{1*}, E. E. Nokhrina¹, I. N. Pashchenko²

¹*Moscow Institute of Physics and Technology, Dolgoprudny, Institutsky per., 9, Moscow region, 141700, Russia*

²*Lebedev Physical Institute, Leninsky prosp. 53, Moscow, 119991, Russia*

Accepted 2023 May 4. Received 2023 May 4; in original form 2023 March 13

ABSTRACT

We examine the effect of a jet transversal structure from magnetohydrodynamic semi-analytical modelling on the total intensity profiles of relativistic jets from active galactic nuclei. In order to determine the conditions for forming double- and triple-peaked transverse intensity profiles, we calculate the radiative transfer for synchrotron emission with self-absorption from the jets described by the models with a constant angular velocity and with a total electric current closed inside a jet. We show that double-peaked profiles appear either in the models with high maximal Lorentz factors or in optically thick conditions. We show that triple-peaked profiles in radio galaxies constrain the fraction of the emitting particles in a jet. We introduce the possible conditions for triple-peaked profiles under the assumptions that nonthermal electrons are preferably located at the jet edges or are distributed according to Ohmic heating.

Key words: MHD – radiation mechanisms: nonthermal – radiative transfer – galaxies: jets – quasars: general

1 INTRODUCTION

Relativistic jets from active galactic nuclei (AGN) are thought to originate in the vicinity of supermassive black holes (SMBH) having angular momentum (spin) and accreting matter from the ambient medium (Blandford et al. 2019). Relating the observations of jets on parsec scales in radio and millimeter band to the physics underlying AGN activity and jet production requires more or less elaborate modelling of jet and emitting plasma properties. The Blandford–Königl model (Blandford & Königl 1979) employs the assumption of equipartition of emitting plasma energy density with the proper magnetic field energy density (Burbidge 1956). The model assumes the certain dependencies of particle number density and magnetic field on the distance from the jet base. Despite neglecting the jet transversal stratification, this model was successful in explaining such observational phenomena as core shift effect (Kovalev et al. 2008). The Blandford–Königl model was used to estimate the jet magnetic field and plasma number density (Lobanov 1998; Hirotani 2005; O’Sullivan & Gabuzda 2009; Nokhrina et al. 2015), although for extreme brightness temperatures a proper accounting for the non-uniform jet structure is needed (Nokhrina 2017). At the same time, theoretical and numerical modelling of non-uniform jets within the approach

of ideal magnetohydrodynamics (MHD) progressed to reproducing plasma bulk acceleration up to relativistic velocities (Beskin & Nokhrina 2006; Komissarov et al. 2009; Lyubarsky 2009; Tchekhovskoy et al. 2009) and a jet boundary shape (Chatterjee et al. 2019; Nokhrina et al. 2019; Kovalev et al. 2020).

The recent jet observations by the very-long-baseline interferometry (VLBI) method in radio band allow us to look at the jets down to the event horizon scales (Event Horizon Telescope Collaboration et al. 2019a,b). These observations reveal the clear jet stratification in intensity with a pronounced limb brightening in Mrk501 (Giroletti et al. 2004), M87 (Walker et al. 2018), 3C 84 (Giovannini et al. 2018) and Cen A (Janssen et al. 2021); transition from spine to limb brightening at different frequencies in 3C 273 (Bruni et al. 2021) and even a triple-peaked emission structure in the core region in M87 (Hada 2017) which is detected down to the scales of a few gravitational radii (Lu et al. 2023).

There may be several reasons for the observed stratified emission from relativistic jets. The stratified poloidal velocity field may lead to boosting and de-boosting of emission from different parts of a jet. In particular, in the models with fast spine and slow sheath, limb brightening may occur due to de-boosting of emission from a sheath, while the emission from a fast relativistic spine is concentrated in the narrow angle around the bulk plasma velocity, and we do not observe this emission. Another possible source of a stratified

* E-mail: frolova.va@phystech.edu

emission is a spatial distribution of nonthermal electrons. We assume that the synchrotron self-absorbed emission is produced by the relativistic plasma with energy distribution given by the power law

$$dn_{\text{emit}} = k_e(\mathbf{r})\gamma^{-p}d\gamma, \quad (1)$$

where γ is a particle Lorentz factor, n_{emit} is emitting plasma number density with the amplitude k_e depending on the coordinate \mathbf{r} within a jet, p is a power law index related to the spectral index $\alpha = (1-p)/2$ of the synchrotron emission optically thin regime spectral flux

$$S_\nu \propto \nu^\alpha. \quad (2)$$

Such distribution may be produced by the acceleration on shocks (e.g., [Kirk et al. 1994](#)) by the Fermi mechanism of the first order or by the magnetic reconnection ([Sironi et al. 2013](#)) with subsequent appearance of region with an electric field larger than a magnetic one, where charged particles accelerate effectively. These processes may take place locally, for example, at the jet boundary due to developing instabilities (e.g. pinch instabilities shown by [McKinney \(2006\)](#); [Chatterjee et al. \(2019\)](#), Kelvin-Helmholtz instability (e.g. [Hardee & Eilek 2011](#), [Nikonov et al. submitted](#))). The power-law spectrum can also be produced by shear acceleration when the particles gain energy crossing the tangential velocity discontinuity at the jet boundary due to diffusion, if the velocity jump is relativistic and the turbulence is present ([Ostrowski 1990, 1998](#)). So, nonthermal electrons may also be distributed non-uniformly across a jet, giving rise to peculiar structures in intensity and spectral maps (e.g. [Nikonov et al. submitted](#), [Bruni et al. 2021](#)). Non-uniform distribution of nonthermal electrons could be also due to possible particle acceleration as a result of Ohmic heating, so that the amplitude k_e is proportional to the square of co-moving electric current density j'^2 ([Lyutikov et al. 2005](#)), or due to the equipartition regime between plasma and magnetic field, so that k_e is proportional to the square of proper magnetic field B'^2 ([Burbidge 1956](#); [Blandford & Königl 1979](#)). One more reason may be a non-uniform jet structure itself: as the emission and absorption coefficients depend on a local magnetic field and particle number density, variation in these physical values leads to variations in emission. This approach has been used to estimate the magnetic field in a jet by the observed brightness temperature ([Nokhrina 2017](#)). Another possible reason of the observed stratification is the opacity effect. [Zakamska et al. \(2008\)](#) considered a “core-dominated” jet with optically thick geometrically thin core and a surrounding optically thin jet. It was shown that the observed transverse structure could significantly depend on frequency. Observations of quasar 3C 273 with RadioAstron at 1.6 and 4.8 GHz by [Bruni et al. \(2021\)](#) revealed the effect of a frequency-dependent intensity profile. The jet from 3C 273 is limb-brightened at 1.6 GHz and is spine-brightened at 4.8 GHz, with a clear spectral index gradient across the jet. Authors considered several concurring factors that could explain the observed picture, including plasma stratification across the jet. There is also a possibility that many of these effects contribute to the observed emission profiles (see, e.g., [Gabuzda 2021](#)).

To model observed intensity profiles from M87 jet, steady axisymmetric force-free jet models have been suc-

cessfully employed. [Broderick & Loeb \(2009\)](#) used the Gaussian distributions of both thermal and nonthermal electrons and showed that limb brightened intensity profiles emerge in the case of high black hole (BH) spin, and low spin produces one-peaked, highly asymmetric profiles. Setting the Gaussian distribution of emitting electrons at jet’s base in the form of a ring, [Takahashi et al. \(2018\)](#) showed that the symmetrical intensity profiles require a fast-spinning BH as well, and [Ogihara et al. \(2019\)](#) reproduced the triple-peaked intensity profile for the optically thin jet. Relativistic and general relativistic magnetohydrodynamical (RMHD and GRMHD) simulations are also used for modelling M87 intensity profiles. Within GRMHD simulations, [Mościbrodzka et al. \(2016\)](#) obtained a limb-brightened intensity profile using the Monte-Carlo technique developed for relativistic radiative transfer. RMHD simulations by [Fuentes et al. \(2018\)](#) show the three-peaked profiles for the models with high magnetization. [Kramer & MacDonald \(2021\)](#) explored different magnetic field morphologies and electron distributions using 3D RMHD simulations and found out that the jets with purely toroidal and poloidal magnetic fields are limb-brightened and spine-brightened correspondingly, while the electron distributions set proportional to thermal, internal and magnetic energy densities produce similar results. The equipartition between the magnetic and thermal pressure was assumed. Though the intensity profiles patterns are commonly reproduced, the realistic, self-consistent magnetic fields and electron number densities are not well studied.

Analytical and semi-analytical magnetohydrodynamical (MHD) models ([Beskin & Malyshekin 2000](#); [Beskin & Nokhrina 2006](#); [Beskin et al. 2017](#)) provide stationary distributions of physical parameters: velocity, magnetic field \mathbf{B} , particle number density n . We should emphasize that n obtained within this approach is a total (cold) particle number density. The emission and absorption coefficients depend on the nonthermal emitting particle number density $n_{\text{emit}} \leq n$ with the assumed power law energy distribution (1). The particular value of n_{emit} depends on the model assumptions. However, all the physical quantities obtained within the axisymmetrical stationary MHD approach do not depend on time, have smooth distributions and, thus, can be easily used in the numerical calculation of the radiative transfer equation. We use two models described by [Beskin & Nokhrina \(2006\)](#); [Lyubarsky \(2009\)](#) and by [Beskin et al. \(2017\)](#). Both models predict the jet properties in very good agreement with the numerical modelling by [Komissarov et al. \(2007\)](#) and by [Chatterjee et al. \(2019\)](#).

Using the modelled emission profiles, we explore their dependencies on such parameters as a viewing angle, separation from the central engine, total magnetic flux and light cylinder radius. We examine the contributions to the intensity profiles made by the Doppler factor, jet stratification and different distributions of relativistic plasma across a jet. Our objective is to explain the most probable origins of peculiarities observed in jets and to constrain the possible models for nonthermal electrons spatial distribution.

The paper is organized as follows. In [section 2](#) we discuss the chosen models and explain the key principles used to carry out the simulations. Then, we present achieved results in [section 3](#) focusing on the explanation of what profiles

should appear with the use of the models in consideration and on the intensity profiles dependencies on the models parameters. In [section 4](#), the possible model modifications for limb brightening production are discussed. In [section 5](#), we compare our results to the works by other authors and specifically to Blandford-Königl model. Finally, we summarize our work in [section 6](#).

2 APPROACH

2.1 Two models of a jet transversal structure

To model jet synchrotron emission, we use the resultant jet structure obtained within the approach of stationary axisymmetric magnetohydrodynamics. The distribution of magnetic field \mathbf{B} , particle number density n and bulk Lorentz factor Γ are governed by Grad-Shafranov and Bernoulli equations. We assume the electron-positron jet composition ([Zdziarski et al. 2022](#); [Zdziarski & Egron 2022](#)). The solution depends on the particular choice of five quantities, conserved on magnetic surfaces $\Psi = \text{const}$, where Ψ is magnetic flux, — integrals of energy density flux $E(\Psi)$, angular momentum density flux $L(\Psi)$, angular velocity $\Omega_F(\Psi)$, particle density flux to magnetic field ratio $\eta(\Psi)$ and entropy $s(\Psi)$ (see details in [Beskin 2010](#)). After the choice of integrals and for the highly collimated flows we can use the cylindrical approach, so the Grad-Shafranov and Bernoulli equations reduce to the set of ordinary differential equations. The particular solution depends on the integrals choice, and we employ two models. The first one (M1) describes a jet with a constant angular velocity $\Omega_F(\Psi) = \Omega_0$ and linear energy and angular momentum integrals (see the particular integrals choice in [Beskin & Nokhrina 2006](#); [Lyubarsky 2009](#)). The distribution of physical quantities across a jet are presented in Figures 3–4 by [Nokhrina et al. \(2015\)](#) and are in good agreement with the numerical modelling by [Komissarov et al. \(2007\)](#); [Bromberg & Tchekhovskoy \(2016\)](#).

As the second model (M2) we use the model by [Beskin et al. \(2017\)](#). It consists of a central part of a flow alike the Model 1. But due to the special choice of the integrals

$$\Omega_F(\Psi) = \Omega_0 \sqrt{1 - \Psi/\Psi_0}, \quad (3)$$

$E(\Psi)$ and $L(\Psi)$, the model has a slower sheath — a mildly to non-relativistic outflow around a fast central part. The distributions of physical quantities are presented in Figures 1–5 in [Chernoglazov et al. \(2019\)](#). In both models the jet boundary is set as a radius, at which the magnetic flux becomes equal to the total magnetic flux Ψ_0 contained in a jet.

These models describe identically the central part of a jet, where the field lines angular velocity Ω_F is almost constant. Below r denotes the cylindrical radius.

1. Central core, $r < a \text{ few } R_L$.

The central dense core is a part of a jet with the radius of several light cylinder radii $R_L = c/\Omega_F$. It characterizes by almost constant particle number density, which is highest across a jet, and a uniform poloidal magnetic field ([Komissarov et al. 2007](#); [Beskin & Nokhrina 2009](#); [Lyubarsky 2009](#)). Here c is the speed of light. The toroidal magnetic field in the central core is less than or comparable to the poloidal magnetic field, and the flow bulk

Lorentz factor is equal to the initial Lorentz factor Γ_{in} , as this part of a jet remains plasma-dominated from the base. Presence of such a dense jet core is a robust feature of both analytical and numerical models, and it is important to understand its impact on the overall jet emission and possible limitations on the location of nonthermal emitting electrons.

2. Intermediate part, $r < a \text{ few } R_L$ and $\Psi < \Psi_0/2$.

Outside this central core and for the field lines with constant angular velocity, which is present in both M1 and M2 (up to $\Psi \approx \Psi_0/2$), poloidal B_P and toroidal B_φ magnetic fields and a particle number density n decrease with the radial distance while the flow accelerates. This leads to a drop in emissivity and in plasma absorption, and to the strong boosting of emission within a small cone with half-opening angle $\sim \Gamma^{-1}$ around the bulk motion velocity direction.

3. Outer part, $\Psi > \Psi_0/2$.

Within M1, the acceleration continues up to the jet boundary with $\Psi = \Psi_0$, where the highest Lorentz factor is achieved by the flow. The values of n and B are the decreasing functions of r . In contrast, in the M2 the flow bulk velocity decreases towards the jet boundary, leading to emission de-boosting. Particle number density rises abruptly at the boundary (see Figure 1 by [Chernoglazov et al. 2019](#)) as it is the thermal pressure that balances the ambient medium pressure in the M2. So we expect to explore the impact of slower velocity in producing the limb-brightening effect, observed in different sources. The same qualitative behaviour of a bulk Lorentz factor, as in the M2, has been obtained in the numerical simulations by [Chatterjee et al. \(2019\)](#): the flow becomes slower towards the jet boundary, and the Lorentz factor peaks closer to the jet axis relatively to the jet width as compared with further jet cross-sections.

We use the following prescription on the emitting plasma particle number density n_{emit} . In Section 3 we assume that all the plasma from MHD modelling has a power-law distribution (1) and emits, thus $n_{\text{emit}} = n$. This is done in order to capture the impact of the jet stratification on the total intensity profiles. In Section 4 we set the emitting plasma number density proportional to the magnetic field energy density ([Burbidge 1956](#); [Blandford & Königl 1979](#); [Lobanov 1998](#)) and to the electric current density in the proper plasma frame ([Lyutikov et al. 2005](#)).

2.2 Calculating the emission profiles

The problem is considered within the cylindrical approach: we model different intensity profiles across a jet assuming it to be a cylinder with no physical quantities evolution along a jet. This approach works well for the optically thick regimes, as the jet longitudinal evolution is very slow. For optically thin parts of a jet observed at large enough observational angles, the cylindrical approach also is a good approximation, as the profile is formed from the emission of nearby jet slices. In a case of an optically thin jet observed at small angle such approach cannot be applied to modelling the particular jet emission profile, but is aimed to catch the robust features of an emission independently of any model for a longitudinal jet evolution.

To compute the transverse intensity profile, the radiative transfer equation for the synchrotron emission with self-absorption is numerically solved. The radiative transfer

equation in the observer frame has the form

$$\frac{dI_\nu}{ds} = j_\nu - \kappa_\nu I_\nu, \quad (4)$$

where I_ν is the spectral intensity, j_ν and κ_ν are the spectral emission and absorption coefficients, and the equation is solved along the line of sight.

The synchrotron emission and absorption coefficients are written in the plasma proper frame as follows (Ginzburg & Syrovatskii 1965):

$$j'_{\nu'} = h(p) \frac{e^3}{mc^2} \left(\frac{3e}{2\pi m^3 c^5} \right)^{(p-1)/2} \frac{K}{4\pi} B_\perp'^{(p+1)/2} \nu'^{(1-p)/2}, \quad (5)$$

$$\kappa'_{\nu'} = g(p) \frac{e^2}{2\pi m} \left(\frac{3e}{2\pi m^3 c^5} \right)^{p/2} K B_\perp'^{(p+2)/2} \nu'^{-(p+4)/2}, \quad (6)$$

where

$$h(p) = \frac{\sqrt{3}}{p+1} \Gamma\left(\frac{3p-1}{12}\right) \Gamma\left(\frac{3p+19}{12}\right), \quad (7)$$

$$g(p) = \frac{\sqrt{3}}{4} \Gamma\left(\frac{3p+2}{12}\right) \Gamma\left(\frac{3p+22}{12}\right). \quad (8)$$

Here $K = k_e(mc^2)^{p-1}$, e is the electron charge, m is the electron mass, B_\perp' is the magnetic field component perpendicular to the wave vector, Γ is gamma function. All the primed quantities and k_e are in the plasma proper frame. The emission and absorption coefficients are recalculated to the lab frame using the Lorentz invariants I_ν/ν^3 , j_ν/ν^2 and κ_ν/ν (Rybicki & Lightman 1979). The proper and observed frequencies ν' and ν correspondingly are related via

$$\frac{\nu'}{\nu} = \frac{1+z}{\delta}, \quad (9)$$

where z is cosmological redshift of the source and δ is Doppler factor. As we intend to describe close, well-resolved sources, we omit z .

The distribution (1) is integrated to express the amplitude k_e in terms of the emitting particle number density n_{emit} :

$$k_e = \begin{cases} \frac{(p-1)n_{\text{emit}}}{\gamma_{\min}^{1-p} - \gamma_{\max}^{1-p}} \approx (p-1)\gamma_{\min}^{p-1} n_{\text{emit}}, & p \neq 1, \\ \frac{n_{\text{emit}}}{\ln \gamma_{\max}/\gamma_{\min}}, & p = 1. \end{cases} \quad (10)$$

For short, we further denote

$$n_{p,\gamma_{\min}} = (p-1)\gamma_{\min}^{p-1} n_{\text{emit}}. \quad (11)$$

In the calculations, the minimal Lorentz factor γ_{\min} is set equal to unity (Wardle et al. 1998), and the maximal Lorentz factor γ_{\max} is neglected as $\gamma_{\max}^{1-p} \ll 1$. The value of p can be determined for a particular source from observations but its theoretical evaluation is under discussion. From a theoretical perspective the numerical particle-in-cell simulations are used to explore the possible values of p . For relativistic reconnection, they predict the values between 1.5 and 4, with larger values for lower magnetizations (Sironi & Spitkovsky 2014; Ball et al. 2018). On the other hand, for particle acceleration in shocks, they provide ≈ 2.5 for low magnetizations (Sironi & Spitkovsky 2011). Hybrid fluid-particle simulations can help to estimate p as well (e.g.

Vaidya et al. 2018, Kramer et al. in prep.); Vaidya et al. (2018) got the mean of $p \sim 3.1$ in their simulations. Observationally, Pushkarev & Kovalev (2012) obtained the median spectral index in jets of 319 sources $\alpha = -0.68$ between 2 and 8 GHz. Hovatta et al. (2014) found the mean spectral index in the jets of 190 AGNs $\alpha = -1.04 \pm 0.03$ with more flattened spectrum in jet components using four frequency VLBA observations between 8 and 15 GHz. Recently, Pashchenko et al. (2023) employed multifrequency VLBI simulations with relativistic jet model and found that the imaging procedure traditionally used for obtaining the spectral index maps from the VLBI data could artificially steepen the spectrum. Simulations also revealed that the intrinsic optically thin spectral index $\alpha = -0.5$, corresponding to $p = 2$, is consistent with recent dual frequency (8 and 15 GHz) high-sensitivity VLBI observations of M87 radio jet (Nikonov et al. submitted). In the work, the value $p = 2$ is selected as the basic value for certainty.

With $\gamma_{\min} = 1$ and $p = 2$, the expression (10) is simply $k_e = n_{\text{emit}}$.

2.3 Setting the model parameters

Our modelling depends on the following intrinsic parameters.

Firstly, the MHD modelling provides the cross-sections of the jet. The calculated physical quantities are the functions of the radial coordinate r only, since the equations are solved within the cylindrical approach. For the chosen model, M1 or M2, the cross-section is defined by the initial magnetization σ_M and dimensionless radius d_{RL} in the units of R_L . Initial magnetization defines the plasma terminal velocity. Dimensionless jet width is connected with the jet boundary geometry: larger jet radii in terms of a light cylinder radius correspond to larger distances along a jet. On the other hand, larger given jet width at the cross-section corresponds to smaller R_L or, equivalently, a transverse size of a central core.

To solve the radiative transfer equation we must use the dimensional variables. For the particle number density n and the magnetic field B the relation is as follows:

$$n = \tilde{n} \left(\frac{\Psi_0}{8\pi^2 R_L^2 \sigma_M} \right)^2 \frac{1}{mc^2}, \quad (12)$$

$$B = \tilde{B} \frac{\Psi_0}{2\pi \sigma_M R_L^2}, \quad (13)$$

where the dimensionless quantities are denoted with the tilde. Here the light cylinder radius can be related to the BH spin, and the combination of R_L and Ψ_0 can be used to estimate the jet power.

The total magnetic flux Ψ_0 defines the optical thickness of the source (the part of jet under consideration) at a given frequency, and characterises the following jet parameters:

- i. the optical depth τ of the source at a given frequency;
- ii. the part of the cross-section mostly contributing to the intensity – the position of the $\tau = 1$ surface in the jet;
- iii. the spectral index between the pair of frequencies.

All these quantities are strongly stratified. Due to the central core-defined jet structure, these values possess the extrema

in the central part of the jet; the extrema are shifted from the precise jet spine due to the rotation.

As we fix the jet local physical width, the light cylinder radius and the initial magnetization, we have only the total magnetic flux Ψ_0 to vary. We choose the particular values of Ψ_0 to fix the maximum of the optical depth τ_{\max} for the given cross-section. We prefer the optical depth since it is the Lorentz invariant and it is the only stratified characteristic whose transverse profile does not change with Ψ_0 . Moreover, this way of fixing Ψ_0 can be applied independently of the model: though the order of Ψ_0 corresponding to the particular τ_{\max} values differs strongly depending on the (M, d_{R_L}, σ_M) tuple, the optical depth itself stays the universal physical characteristic of a source. Thus, the profiles are indexed with the maximum optical depth value, and the corresponding total magnetic flux and jet power will be listed in the table. The maximum optical depth is varied over the whole range covering optically thin and optically thick options – we tried 15 values from 0.01 to 500, and we chose 8 values from this set to present in the plots in the paper. The total magnetic flux Ψ_0 is also related to the jet power, which can be calculated via the Poynting flux power at the jet base (Nokhrina 2018):

$$W_{\text{jet}} = \frac{c}{8} \left(\frac{\Psi_0}{\pi R_L} \right)^2. \quad (14)$$

In our study we focus on understanding of impact of a jet stratification and different models of the spatial distribution of nonthermal plasma on the total intensity profiles. In order to capture general features, we keep the number of the parameters that we vary as small as possible. To address the jet viewing angle, we choose two values of 5° and 15° . They are typical for BL Lacs/quasars/blazars and radio galaxies without a pronounced counter-jet correspondingly (Pushkarev et al. 2012; Lister et al. 2018, 2019; Kovalev et al. 2020). The value 15° is also preferable as it lies in the interval of estimated viewing angle for M87 between 14° and 19° (Nakamura & Meier 2014; Mertens et al. 2016; Walker et al. 2018; Nakamura et al. 2018; Kim et al. 2018), which is especially interesting source with the best resolved transversal and longitudinal structure in intensity. Below we refer to the sources with these two viewing angles as ‘BL Lacs/quasars/blazars’ and ‘radio galaxies’ meaning only the typical viewing angle, and not the real source type.

For initial magnetization σ_M , Nokhrina et al. (2022) showed that $\sigma_M \approx 2\Gamma_{\max}$ and $\Gamma_{\max}/2$ for M1 and M2 correspondingly. Thus, for M1, considering M87 as an example, $\sigma_M = 5; 20$ are selected as reference values according to $\Gamma \sim 3$ at small scales reported by Mertens et al. (2016) and $\Gamma \sim 10$ at larger scales reported by Biretta et al. (1999). $\sigma_M = 50$ is chosen as well to demonstrate the higher velocities effects. For blazars, Lorentz factors are estimated to be up to 50 using VLBI kinematics (Lister et al. 2019), so the chosen value can be taken into account in the qualitative considerations. For M2, the corresponding values are modified to maintain the upper velocity limit. The precise Γ_{\max} at the considered jet cross-sections are given in Table 1.

To set R_L , two characteristic cross-sections are considered: with the central core taking up i. nearly all the jet width; ii. only the small fraction of the jet width. This is done to explore the impact of a central core on the overall intensity map, as it occupies the scales of several R_L

Model	σ_M	d_{R_L}	Γ_{\max}
M1	5	25	4.0
M1	5	100	4.4
M1	20	25	9.9
M1	20	100	13.4
M1	50	25	15.0
M1	50	100	25.9
M2	5	25	3.1
M2	5	100	3.7
M2	20	25	6.6
M2	20	100	10.4
M2	50	25	9.0
M2	50	100	18.5

Table 1. The maximum Lorentz factor Γ_{\max} on the cross-sections considered in the paper.

(Beskin & Nokhrina 2009). For certainty, for every model under consideration we choose the universal values $d_{R_L} = 25; 100$. These values are treated in two different ways: i. the geometrical width is kept, so the central core impact is explored; ii. the light cylinder radius is kept, so the separation from the central engine is explored.

The geometrical jet width is set to 0.5 pc and the luminosity distance 0.1 pc/mas is used for the spectral flux calculation. This fiducial choice aims to provide the outcome expected from the considered models for the nearby resolved on the sub-parsec scales AGN jets. For M87, the closest and best resolved source, the luminosity distance is 0.08 pc/mas and the sub-parsec jet is few mas wide.

This choice is not restrictive. Suppose rescaling the jet width, in pc, as $d' = ad$ and examining the same model cross-section of the jet. The profile contours at the same optical depths, but at R_L and $R'_L = aR_L$ are almost indistinguishable to the central core profoundness, and the primary difference is the intensity values. The intensity can be approximately recalculated from the homogeneity assumption after equating τ for R_L and R'_L :

$$I' \approx a^{1/(p+6)} I. \quad (15)$$

Now suppose rescaling the observed jet width, in mas, as $d' = ad$ and examining the same cross-section of the jet. If the intensity profile is divided into the same number of pixels, then each of them is seen at the solid angle $\Omega' = a^2\Omega$, so

$$I' = a^2 I. \quad (16)$$

The total magnetic flux Ψ_0 is expected to have the order of $10^{33} - 10^{34}$ G cm² (Zamaninasab et al. 2014). As we choose the model parameters as described above, total magnetic flux Ψ_0 is not predetermined, but chosen in order to achieve the particular value of the optical depth in the central part of the jet. Thus, we analyse and compare its values *a posteriori*.

The jet rotation is responsible for asymmetries in the intensity profiles, and we plot the advancing side of a jet to the left, and the receding part of a jet to the right.

The model parameters are summarized in Table 2.

Parameter	Tried values
Model	M1, M2 (see subsection 2.1)
σ_M	5, 20, 50
θ	5°, 15°
(d_{R_L}, R_L) (‘ R_L comparison’ mode)	(25, 0.01 pc), (100, 0.025 pc)
(d_{R_L}, R_L) (‘evolution’ mode)	(25, 0.01 pc), (100, 0.01 pc)

Table 2. The parameters used for intensity profiles modelling.

3 SPECTRAL INTENSITY TRANSVERSE PROFILES

In this section, we present the modelling of spectral intensity profiles on the (M, σ_M, d_{R_L}) tuples and discuss the robust features of emission from MHD jets when relativistic plasma has the same energy distribution across a jet. In [section 4](#), we explore the effects of non-uniform spatial distribution of radiating plasma.

3.1 ‘ R_L comparison’ mode

In [Figures 2](#) and [3](#) we present the intensity profiles plot sets in the ‘ R_L comparison’ mode: the geometrical jet width is set to the same value $d_{\text{jet}} = 0.5$ pc for every plot, so different d_{R_L} values relate to different R_L values. For the magnetic field lines threading the BH ergosphere, the condition of a maximum jet power $\Omega_F = \Omega_H/2$ can be used ([Blandford & Znajek 1977](#)), although there are some indications of Ω_F being much lower than the BH angular velocity Ω_H ([Nokhrina et al. 2019](#); [Kino et al. 2022](#)). In this case, the light cylinder radius can be related to the dimensionless BH spin a^* according to the expression ([Mertens et al. 2016](#); [Nokhrina et al. 2020](#))

$$|a^*| = \frac{8a}{1 + 16a^2}, \quad a = \frac{r_g}{R_L}, \quad (17)$$

where r_g is the gravitational radius. We plot the dependence of a^* on R_L in [Figure 1](#) having chosen M87 as a reference example. We regard only the absolute values of BH spins as the positive and negative values and indistinguishable within our approach. Down to $4r_g$ the smaller light cylinder radii correspond to higher BH spins, so we compare the jets from BHs with different spins while comparing R_L values. Thus, ‘ R_L comparison’ mode attitude aims to determine how wide or narrow transversely should be the central core to describe a particular given cross-section of the jet.

The plot sets are splitted in two major parts, upper and lower, dedicated to each of M1 and M2; σ_M , i.e. terminal Lorentz factor, grows along the horizontal axis, and d_{R_L} , i.e. BH spin, grows down the vertical axis. The plot sets are done for the viewing angles 5° ([Figure 2](#)) and 15° ([Figure 3](#)) to capture common features of intensity profiles for quasars and radio galaxies. We show both the ideal, immediate result of the radiative transfer and the smoothed plots, convolved with the round beam of 0.5 mas chosen so to be the order of magnitude less than the preset jet width. The intensity values are expressed in the unities of Jy/pixel, where the pixel is a square with sides of 10^{-4} pc. This pixel is chosen as it is intrinsic in our calculations. In this case, the beam

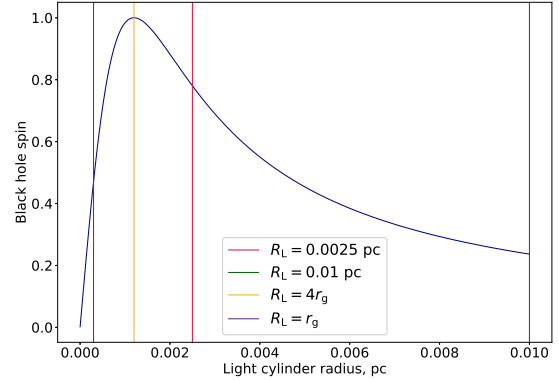


Figure 1. The dependence of the absolute value of a BH spin on the light cylinder radius for M87. The vertical lines indicate our probe values, the gravitational radius and the maximum at $4r_g$.

the order of magnitude less than the preset jet width would contain $\propto 10^6$ pixels.

There is a strong difference in the intensity amplitude for the plots with different optical depth τ_{max} . So, we plot them at the different scales, with the values for $\tau_{\text{max}} \geq 1$ indicated on the left and for $\tau_{\text{max}} < 1$ on the right axis.

1. BL Lacs/quasars/blazars and radio galaxies systematics.

Comparing [Figures 2](#) and [3](#) we observe, that, on average, the quasar intensity distribution is wider than the one in radio galaxies. This is a consequence of boosting of emission from a smaller part of a jet for a larger observational angle.

2. Plasma velocity effects.

The bulk Lorentz factor of a flow in a particular jet model impacts the intensity profile symmetry. Lorentz factors in our plots depend on the initial magnetization σ_M , with slower jets presented in the left column and the faster jets in the right. Moving from lower to higher Lorentz factors, we observe, that the almost symmetrical profiles on the left become strongly asymmetrical on the right. This effect is again due to boosting the plasma emission by the flow with a toroidal velocity of the order of 0.1 c . We also checked the dependence of the intensity profile asymmetry on the viewing angle in the plasma frame that changes with the increase of the Lorentz factor (i.e. relativistic aberration) by considering profiles with different σ_M but artificially setting the zero toroidal velocity and found insignificant effect. The symmetry of an intensity profile depends on both the velocity and the observational angle (compare the second column, first line panel in [Figures 2](#) and [3](#)): the condition $\theta_{\text{obs}} < 1/\Gamma$ demarcates the asymmetric from symmetric profiles.

High Lorentz factors in a jet (panels in the right columns) also lead to the overall offset of intensity towards the approaching part of a jet. In fact, in this case we should observe only one edge of a jet. As in one half of the jet the toroidal field projection is the same, in the polarization measurements this effect should be seen as a Faraday rotation measure (RM) with only one sign. Such RMs are observed in e.g. 3C 78, 4C +40.24, S5 0212+73, 3C 111, DA 406 ([Gabuzda et al. 2017](#)). Thus, observations of one sign RM do not necessarily imply the absence of the toroidal mag-

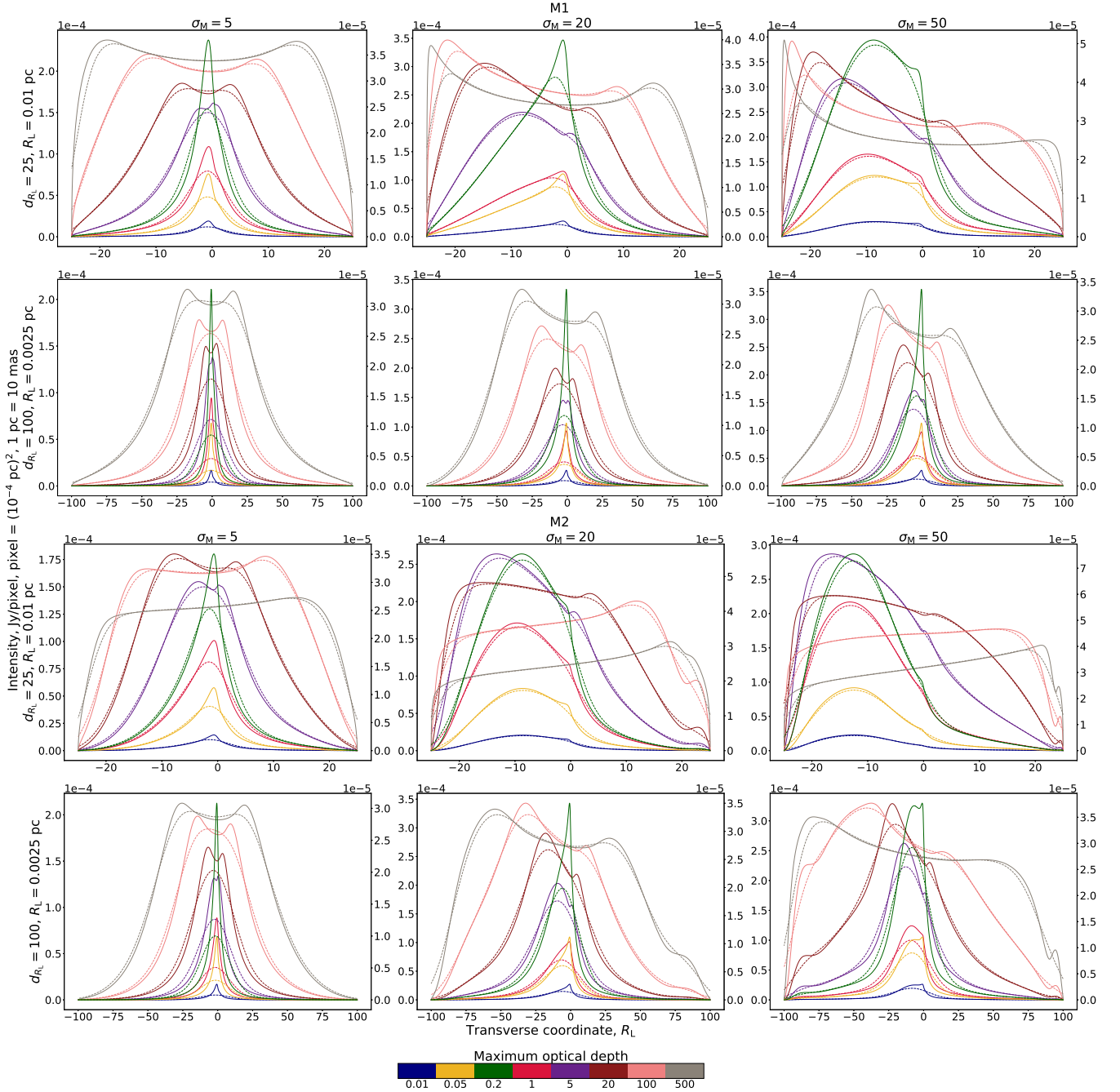


Figure 2. The ideal (solid lines) and convolved (dashed lines) intensity profiles at the viewing angle 5° . The upper and lower plots describe the models M1 and M2 correspondingly (see the models' description in [subsection 2.1](#)). The R_L values are chosen in the 'R_L comparison' mode (the first and second row for each model describe the jet cross-section of the same geometrical width, 0.5 pc, but with different light cylinder radii, see details in the beginning of [section 3](#)). The colours correspond to the maximum optical depth over the cross-section, τ_{\max} . $\tau_{\max} \leq 1$ are plotted at the left y-axis, and $\tau_{\max} < 1$ are plotted at the right y-axis. The convolving beam is round with the FWHM equal to 0.1 of the cross-section width (0.5 mas). The physical parameters for this figure are summarized in [Tables 3 and A1](#).

netic field component in a jet. They could be explained by the shift in emission intensity maximum for high bulk flow Lorentz factors — of the order of 20 and more, while the opposite side of a jet with other sign of magnetic field along a line of sight is not seen due to much lower intensity.

In principle, the influence of the high Lorentz factors on the transverse jet asymmetry could be tested with VLBI observations. However, there are several important issues to

consider. First, as shown in [Pushkarev et al. \(2017\)](#) on a MOJAVE sample a true jet geometry in a considerable fraction of AGNs appears only after stacking single epoch maps over several years. Second, VLBI kinematic measurements could estimate not the true plasma, but the pattern speed, although there are other methods, which require simultaneous multi-frequency VLBI observations (e.g. [Kutkin et al. 2019; Plavin et al. 2019](#)).

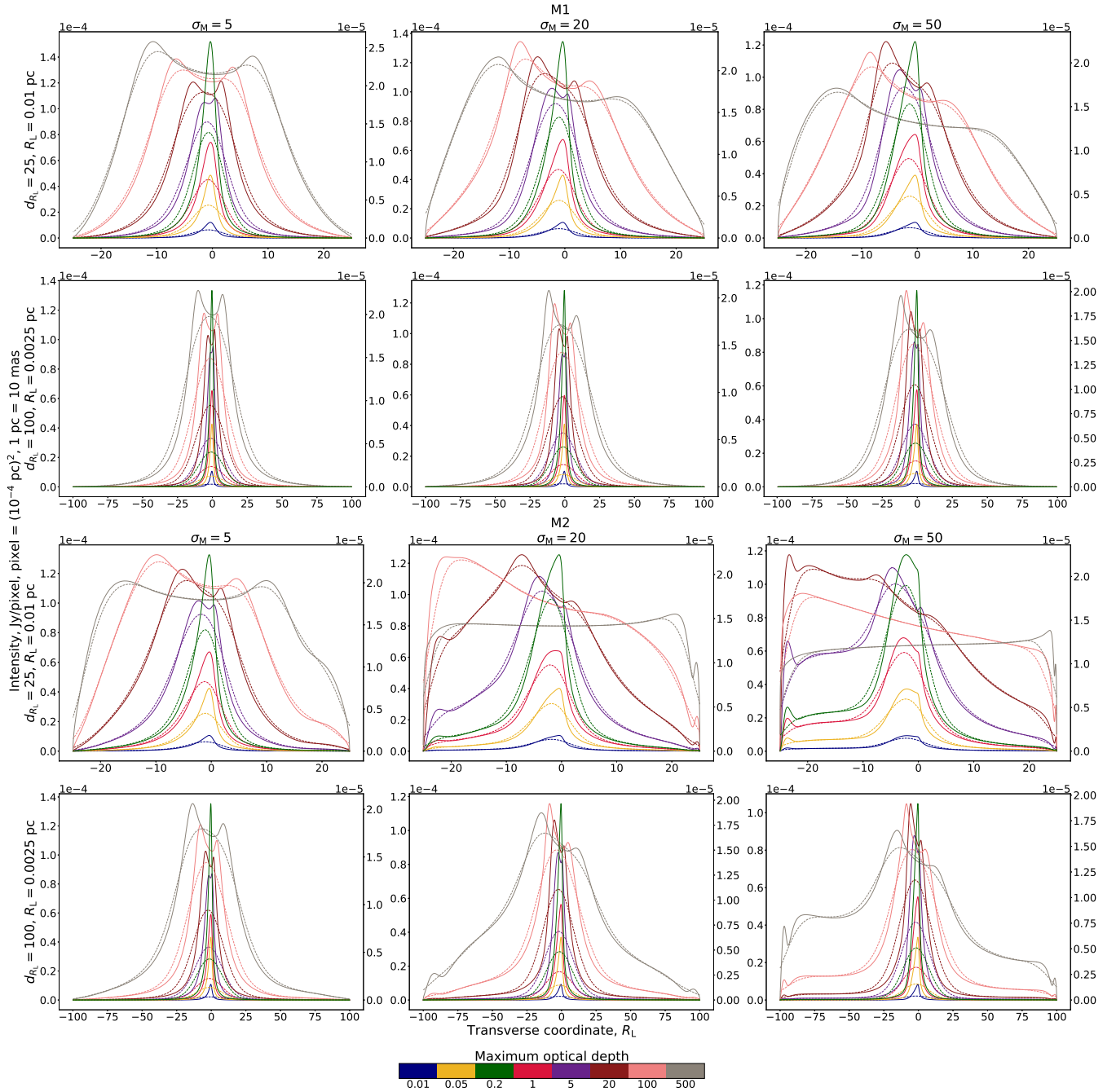


Figure 3. The same as in Figure 2, but at the viewing angle 15° . The physical parameters for this figure are summarized in Tables 4 and A2.

3. Optical depth effects.

Maximum optical depth in Figures 2 and 3 is indicated by the colour. Due to substantial stratification of the jet, the averaged over the cross-section optical depth is noticeably lower than its maximum. For example, for the $d_{R_L} = 25$ cross-sections it is the order of magnitude lower. This means, that maroon curve should roughly correspond to the radio core region. Though the maximum-to-averaged ratio varies from model to model, using maximum values uniformly for all models makes sense for well-resolved sources. In this case, strong transverse gradients in optical depth can manifest themselves, for example, in transverse spectral index gradi-

ents. The illustration for the possible spectral index gradients is given in Figure 4. In the figure, we choose the model (M2, $\sigma_M = 5$, $d_{R_L} = 25$) at 15° , and we plot i. the 15.4 GHz optical depth profile at $\tau_{\max} = 1$ to give the feel of transverse optical depth behaviour, ii. the intensity profiles at 15.4 and 8.4 GHz and iii. the corresponding spectral indices. It is seen that e.g. the spectral index of approximately 1 or 2 in the central part of the jet can be accompanied by optically thin jet edges (see the plots for $\tau_{\max} = 1; 5; 20$).

For optically thin regimes, the emission from the central core dominates the total jet emission. With the growth of optical depth, while the difference between brightened

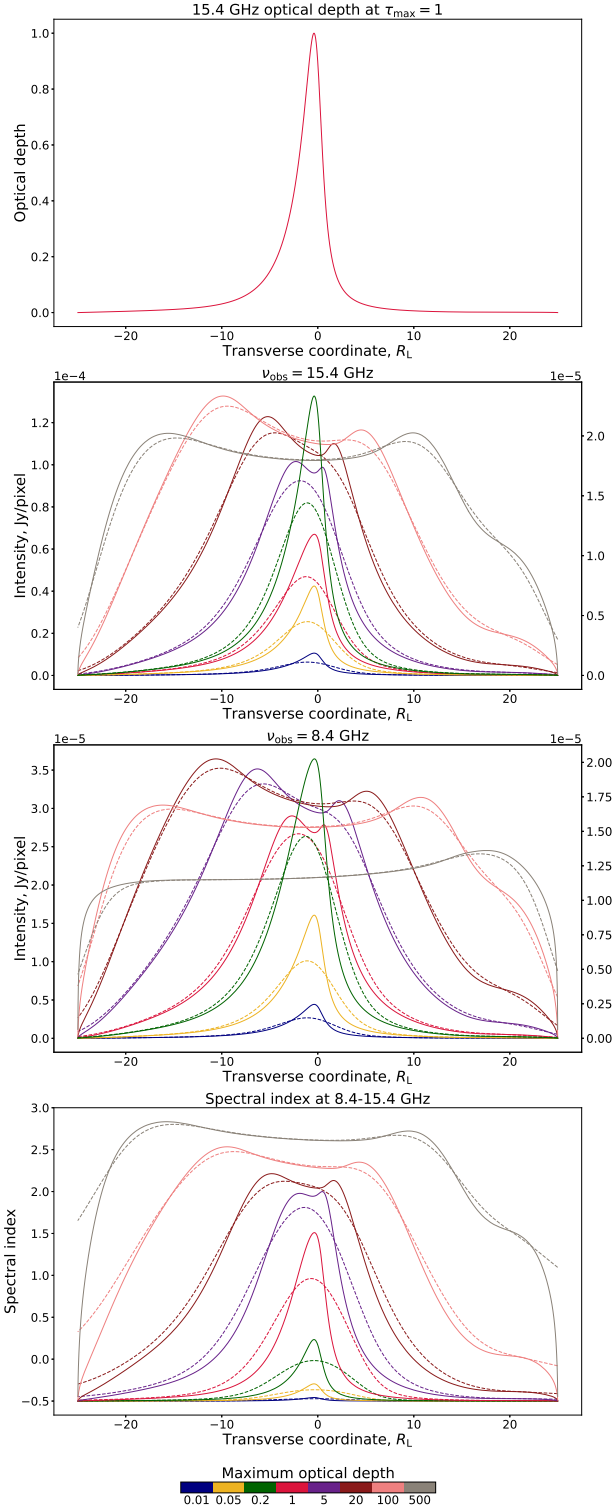


Figure 4. Within (M2, $\sigma_M = 5$, $d_{R_L} = 25$) at 15° , the 15.4 GHz optical depth profile at $\tau_{\max} = 1$ (so it corresponds to the $\tau_{\max} = 1$ 15.4 GHz profiles of the same colour), the intensity profiles at 15.4 (the same as in Figure 3) and 8.4 GHz and the corresponding spectral index. The solid lines are the ideal intensity profiles/the spectral index calculated based on the ideal intensity profiles, the dashed lines are the convolved intensity profiles/the spectral index calculated based on the convolved intensity profiles. The colours correspond to the maximum optical depth over the cross-section, τ_{\max} . $\tau_{\max} \leq 1$ are plotted at the left y-axis, and $\tau_{\max} < 1$ are plotted at the right y-axis. The convolving beam is round with the FWHM equal to 0.1 of the cross-section width (0.5 mas). MNRAS **000**, 1–19 ()

central core and weakly radiating edges becomes less prominent, the net radiation increases drastically. In most cases sufficient optical thickness leads to forming the profile with two maximums (the maximum optical depth of 5 or more), and their profoundness varies with the symmetry. In the observations, the larger optical depth corresponds to the lower observational frequency. Though the dependence on the observational frequency and total magnetic flux are not the same, qualitatively, they are similar. Thus, we predict that the change from a spine-brightened intensity profile to a limb-brightened profile with lowering the observational frequency occurs in low magnetized jets from the BHs with high spins. This could be the case of the observed effect in 3C 273 (Bruni et al. 2021).

On the other hand, in the highly asymmetric intensity profiles optical thickening can result in the change of the brightened edge from one to another (the middle and right panels in the third row corresponding to high magnetization and low BH spin in both Figures 2 and 3). It has the same nature as spine-to-limb brightening transition: the stronger emitting region also absorbs stronger, so at sufficient optical depth it becomes less bright than the region that emits weaker and absorbs weaker. However, this effect is observed only in M2 model due to the presence of a slower sheath around a fast spine. The observational constraints of such effect should help make further conclusions about the presence of a slow sheath and a relatively large light cylinder radius.

4. Impact of a slow sheath presence.

In M2 model the Lorentz factor goes to unity at the boundary, so the outer region of the jet is brightened in highly magnetized jets (the middle and right panels in the third line in Figure 3) as the radiation of outer part of a fast spine is suppressed due to boosting. This effect is hinted in 5° profiles, but more pronounced at the viewing angle 15° . We interpret it as the possible explanation for forming the triple-peaked intensity structure. We expect this structure to be pronounced in highly magnetized jets from the BHs with large enough light cylinder radius and observed at considerably large viewing angles. Particularly, M87 jet is observed at the viewing angle of 17.2 ± 3.3 according to Mertens et al. (2016), and it is likely to possess the large light cylinder radius (Nokhrina et al. 2019). The said conditions are required for the symmetry and for the possibility to produce a clear effect in the optically thin jets.

We also observe (Figure 3, panels in the right column), that the emission de-boosting due to lower velocity towards the jet boundary alone does not lead to the limb brightening, but only to the intensity flattening (see, for example, Figure 3, the purple, green, red curves in the panel in the right column, third line). The flat parts of these curves correspond to already lower Lorentz factor of a bulk plasma motion. The lower plasma number density and smaller magnetic field amplitude in this part of a jet leads to fall in emissivity. Combination of smaller emissivity and emission de-boosting leads to a flat intensity profile. However, as the plasma number density grows closer to a jet boundary (Chernoglazov et al. 2019), together with a low velocity it results in a bump in intensity.

Thus, we conclude, that one can expect the triple-peaked structure across a jet if i. there is a central core manifesting itself the best at the moderate optical depths;

ii. the optically thin jet edges with slow velocity and large particle number density. The latter can be result of matter entrainment from the ambient medium, for example, disk wind (Araudo et al. 2011).

The intensity profiles peaks are somewhat smoothed due the convolution. They are drawn in dashed lines in the same figures. For the chosen beam, the low-scale stratified patterns disappear.

3.2 ‘Evolution’ mode

In the previous subsection, we explored the typical intensity behaviour across a jet for different physical scenarios. In this subsection we want to explore how for every given model the intensity profile closer to the jet base changes as we move along a jet.

The profiles in Figure 5 show how the given $d_{R_L} = 25$ plot is supposed to evolve up to the widths of $d_{R_L} = 50$ and 100. The distance from the central engine grows from left to right, each row corresponds to the particular combination of the model (M1 or M2), initial magnetization σ_M and viewing angle. In this figure, the coloured panel showing the maximum optical depth corresponds to the plot colours at the panels in the first column only. As we move from the panel in the first column to the corresponding panel in the second and then third columns, we keep the model parameters, the observational frequency, and we designate it by using the same colour. For example, three grey curves in the upper row correspond to the same jet model, but for three cross-cuts at different distances from the jet base. As there are no edge effects at larger distances (at $d_{R_L} = 50, 100$), the horizontal axis is cut at $25 R_L$ to make clearer what happens on the same transverse scales.

For the models with lower initial magnetization and relatively small bulk Lorentz factor (the first row in Figure 5), we again observe symmetric intensity profiles and a transition from double-peaked to single-peaked structure as for the maroon line in two left panels for M1.

We propose that the jet stratification may influence the apparent change in a jet position angle (PA) along a jet. We see in the second and third rows of Figure 5, corresponding to $\sigma_M = 50$ and viewing angle 5° in M1 and M2, green (optically thin) curve, that the intensity peak shifts along a jet noticeably. So, even for a straight jet we would observe a gradual shift in a jet PA due to effects of a jet stratification and optical depth. The same effect, though weaker, occurs for larger viewing angle (the fourth and fifth rows). For M87, Nikonov et al. submitted observe a slight change of the jet PA.

Additionally we should note, that, for a optically thin jet the intensity amplitude mostly declines as we move to a larger distances. While for a optically thick jet the intensity amplitude mostly maintains the same order of magnitude.

3.3 Intensity amplitudes and spectral flux

The characteristic total spectral flux in almost all the presented above figures is much larger, than typical values, reported by the MOJAVE catalogue¹ (Lister et al. 2018).

Typical intrinsic brightness temperature is reported to be $(4.1 \pm 0.6) \times 10^{10}$ K (Homan et al. 2021), which is recalculated for 15.4 GHz and e.g. the round beam of 1 mas as approximately 8 Jy/beam. To compare, as we used the MOJAVE frequency 15.4 GHz to construct the plots, consider the maximums of intensity in our $\tau_{\max} = 1$ plots. The maximum intensity amplitude on our plots is of the order of a few 10^{-4} Jy/pixel. Having a beam size of 10^6 pixels, we obtain for a spectral flux values of the order of 100 Jy — several orders of magnitude higher, than the observed values in a jet core region. Only the most optically thin regimes have a spectral flux of a few Jy.

A jet with a structure, obtained self-consistently within ideal axisymmetric stationary MHD approach, has a central core — a dense particle-dominated part with the strongest magnetic field. This feature is robust. However, we observe, that in all the regimes, except for the most optically thick, it is the radiation from this core that dominates the overall jet emission. Thus, all our models have an excess flux as a consequence of accounting for an emission of a central core.

We must conclude, that only a small fraction — of an order of a percent — of total particle number density are the emitting particles. The major part of the plasma is cold and does not emit. This is in agreement with the models of particle acceleration on shocks or in reconnection events (Sironi & Spitkovsky 2011; Sironi et al. 2013; Sironi & Spitkovsky 2014). In this case all the major effects of a jet stratified structure, described above in subsection 3.1, are present, but with the total spectral flux values, closer to the observed ones.

4 OTHER DISTRIBUTIONS OF NONTHERMAL ELECTRONS ACROSS A JET

Using the robust model for the central part of a jet, we obtained a dominance in jet emission of a central core or nearby jet parts. Double-peaked intensity profiles require extremely high optical depths or a combination of high magnetization and considerably large viewing angle. Triple-peaked intensity profiles require even stronger combination: high magnetization, high BH spin and larger viewing angle, as the symmetry is needed to highlight both of the jet edges. Additionally, the said peaks are not pronounced in comparison with the central core-defined peak. The intensity values are also notably higher than we expect for nearby sources, e.g. M87. So, it is likely that the jet transverse structure itself cannot describe the observations. We conclude that the limb brightening can be reconstructed in our modelling only if a jet has a slow sheath with the same order of particle number density and magnetic field, as in the central core. Larger particle number density with small velocity can be connected with a disc wind (Blandford & Payne 1982; Stone et al. 1999; Levinson & Globus 2017; Lu et al. 2023). However, having the same amplitudes of a magnetic field as in the dense core may be problematic. In order to reconcile our findings with the observations, we consider different distributions of the nonthermal (i.e. emitting) plasma.

¹ <https://www.cv.nrao.edu/MOJAVE/index.html>

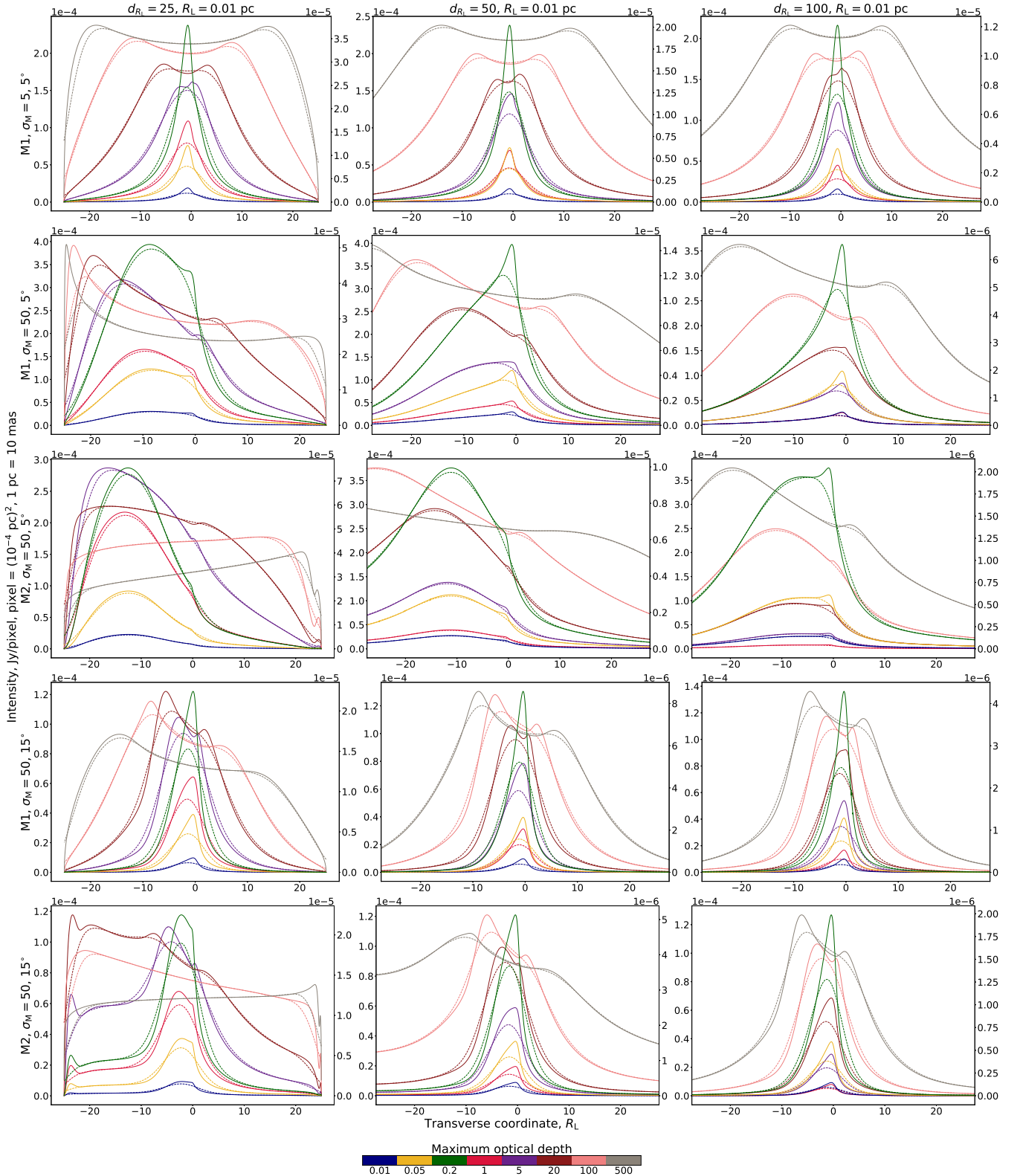


Figure 5. The ideal (solid lines) and convolved (dashed lines) intensity profiles describing the jet at different distances from the central engine; the distance grows from the left to the right; each row corresponds to the particular combination of the model (M1 or M2), initial magnetization σ_M and viewing angle. The colours correspond to the maximum optical depth over the cross-sections in the first column, τ_{\max} . $\tau_{\max} \leq 1$ are plotted at the left y-axis, and $\tau_{\max} < 1$ are plotted at the right y-axis. The convolving beam is round with the FWHM equal to 0.1 of the closest (the first column) cross-section width (0.5 mas). The physical parameters for this figure are summarized in Table B1.

M	σ_M	d_{RL}	$\Psi_0,$ 10^{34} G cm^2	$W_{\text{jet}},$ $10^{44} \text{ erg s}^{-1}$	$n'_{\text{max}},$ cm^{-3}	$n'_{\text{average}},$ cm^{-3}	$B'_{\text{max}},$ G	$B'_{\text{average}},$ G	$I_{\text{max}},$ $\mu\text{Jy/pixel}$
M1	5	25	1.41	0.80	1453	156	0.055	0.014	79.35
M1	20	25	2.51	2.52	807	91	0.069	0.020	103.92
M1	50	25	4.26	7.25	599	71	0.075	0.025	161.21
M1	5	100	0.18	0.20	3717	102	0.069	0.006	29.44
M1	20	100	0.35	0.77	2237	64	0.086	0.009	40.85
M1	50	100	0.65	2.68	1806	54	0.093	0.011	54.46
M2	5	25	0.84	0.28	828	110	0.071	0.020	81.21
M2	20	25	2.44	2.38	507	71	0.082	0.029	166.05
M2	50	25	3.65	5.32	276	40	0.078	0.031	211.80
M2	5	100	0.11	0.08	2195	69	0.088	0.009	35.05
M2	20	100	0.38	0.93	1530	50	0.099	0.012	69.76
M2	50	100	0.80	4.09	1288	44	0.103	0.015	99.94

Table 3. The physical parameters for the maximum optical depth of $\tau_{\text{max}} = 1$ in Figure 2.

M	σ_M	d_{RL}	$\Psi_0,$ 10^{34} G cm^2	$W_{\text{jet}},$ $10^{44} \text{ erg s}^{-1}$	$n'_{\text{max}},$ cm^{-3}	$n'_{\text{average}},$ cm^{-3}	$B'_{\text{max}},$ G	$B'_{\text{average}},$ G	$I_{\text{max}},$ $\mu\text{Jy/pixel}$
M1	5	25	1.77	1.25	2276	244	0.069	0.017	45.17
M1	20	25	3.21	4.12	1322	150	0.088	0.026	46.91
M1	50	25	5.58	12.43	1028	122	0.098	0.033	49.38
M1	5	100	0.22	0.32	5781	159	0.087	0.008	13.80
M1	20	100	0.49	1.54	4485	128	0.122	0.012	14.55
M1	50	100	0.83	4.36	2934	87	0.118	0.014	15.44
M2	5	25	1.06	0.44	1298	172	0.089	0.025	46.90
M2	20	25	3.17	4.02	855	120	0.106	0.038	55.05
M2	50	25	5.75	13.18	685	100	0.122	0.050	59.14
M2	5	100	0.14	0.13	3444	108	0.111	0.011	14.86
M2	20	100	0.49	1.54	2523	82	0.127	0.016	16.70
M2	50	100	1.05	7.00	2202	75	0.135	0.020	17.49
average					2400	130	0.106		
BK					11		0.106		

Table 4. The physical parameters for the maximum optical depth of $\tau_{\text{max}} = 1$ in Figure 3. The last but one line presents the averaged over the models magnetic field and particle number density, and the last line presents the Blandford-Königl model prediction of particle number density for such magnetic field (see section 5).

4.1 Spatial distribution of nonthermal particles

Acceleration of emitting plasma particles on instabilities may be expected preferably in the vicinity of a jet boundary due to developing instabilities (McKinney 2006; Chatterjee et al. 2019; Hardee & Eilek 2011). The Model 1 may be favourable for the shear acceleration at the jet boundary, where the bulk motion Lorentz factor is the greatest across a jet, and plasma with $\Gamma \gg 1$ contacts the ambient medium with non-relativistic bulk velocity (Ostrowski 1990, 1998). In order to account for these effects, we choose the simple Heaviside-like step function with two parameters to describe nonthermal plasma spatial distribution:

$$f(r, k_%, k_r) = \begin{cases} k_%, & r < k_r d, \\ 1, & k_r d \leq r \leq d, \end{cases} \quad (18)$$

$0 < k_{\%,r} < 1$, so $k_%$ stands for the fraction of the particle number density in the central core that is emitting, and $k_r d$ is the radial coordinate, starting from which we assume that all the plasma emits. This function choice implies that the source of nonthermal electrons is due to interaction with the surrounding matter, while the central region does

not undergo such interaction. Discontinuity of the function does not affect the qualitative results but we additionally linearised the transition between two areas, and it can be easily smoothed in other ways. In calculations, we put the renewed k_e function into the general synchrotron emission expressions for emission (5) and absorption (6) coefficients.

The resulting intensity profiles with nonthermal particle spatial distribution $n(r)f(r, k_%, k_r)$ are presented in Figure 6. We chose M2 and $k_% = 0.01$, $k_r = 0.95$ for demonstrative purposes. At 1 per cent of the emitting plasma in a jet dense core, the jets with higher d_{RL} (smaller light cylinder radius; the second row) still possess the prominent central core, while for low d_{RL} (the first row) such suppression of the central core emission is enough to obtain the comparable intensity amplitudes of the center and the edges. We obtain more symmetric distributions for low magnetization and/or smaller light cylinder radius. Thus, we predict that at least one of this conditions is fulfilled for the jets with symmetric triple-peaked intensity profiles: either relatively low Lorentz factors of a flow, or small light cylinder radius (which may correspond to high BH spin).

Therefore, we predict that the interaction with the am-

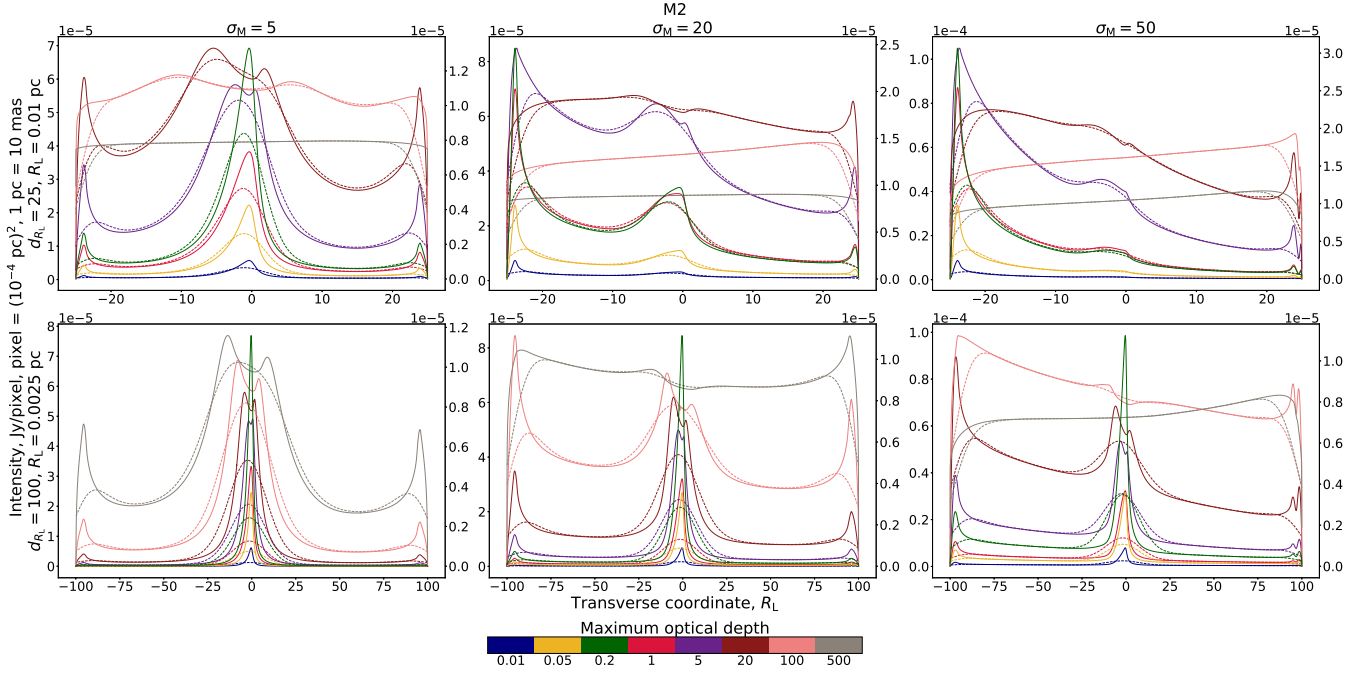


Figure 6. The ideal (solid lines) and convolved (dashed lines) intensity profiles in M2 at the viewing angle 15° for the nonthermal electron distribution defined in (18) with the parameters $k_\% = 0.01$, $k_r = 0.95$. The R_L values are chosen in the ‘ R_L comparison’ mode (the first and second row for each model describe the jet cross-section of the same geometrical width, 0.5 pc, but with different light cylinder radii, see details in subsection 3.1). The colours correspond to the maximum optical depth over the cross-section, τ_{\max} . $\tau_{\max} \leq 1$ are plotted at the left y-axis, and $\tau_{\max} < 1$ are plotted at the right y-axis. The convolving beam is round with the FWHM equal to 0.1 of the cross-section width (0.5 mas). The physical parameters for this figure are summarized in Tables 5 and A3.

M	σ_M	d_{R_L}	Ψ_0 , 10^{34} G cm^2	W_{jet} , $10^{44} \text{ erg s}^{-1}$	n'_{\max} , cm^{-3}	n'_{average} , cm^{-3}	B'_{\max} , G	B'_{average} , G	I_{\max} , $\mu\text{Jy/pixel}$
M2	5	25	3.32	4.40	1507	67	0.281	0.079	27.26
M2	20	25	8.49	28.75	1698	46	0.284	0.101	34.18
M2	50	25	10.06	40.39	919	19	0.214	0.087	41.23
M2	5	100	0.45	1.27	436	22	0.350	0.035	8.41
M2	20	100	1.55	15.35	915	21	0.400	0.050	9.89
M2	50	100	3.30	69.41	1581	22	0.424	0.063	12.21
average					1180	33	0.326		
BK					106		0.326		

Table 5. The physical parameters for the maximum optical depth of $\tau_{\max} = 1$ in Figure 6. The last but one line presents the averaged over the models magnetic field and particle number density, and the last line presents the Blandford-Königl model prediction of particle number density for such magnetic field (see section 5).

bient medium is a key process for the limb brightening appearance in an optically thin jets. In the same time, the central core emission suppression moderates the intensity values in average (compare Tables 4 and 5).

Thus, excluding the spine emission is a promising mechanism for producing the brightened areas close to the jet boundaries, though the particular realisation and extent of the effect are under question. We note that other similar mechanisms of excluding the emission from the central region are considered, e.g. in Cruz-Orsorio et al. (2022) and Fromm et al. (2022) the emitting jet sheath and non-emitting jet spine are separated basing on the local magnetization.

4.2 Ohmic heating

In this subsection we want to show how other assumptions on the nonthermal plasma spatial distribution affects the intensity profiles of synchrotron radiation from the stratified jets.

It was shown by Lyutikov et al. (2005), that the observed jet linear polarization for specially chosen magnetic field and particle number density distributions across a jet is consistent with the following distribution: $k_e \sim j'^2$. Here j' is an electric current density in the plasma proper frame, which essentially implies Ohmic heating. Since

$$j_z = \frac{c}{4\pi r} \frac{\partial(rB_\varphi)}{\partial r}, \quad (19)$$

$$j_\varphi = -\frac{c}{4\pi} \frac{\partial B_z}{\partial r}, \quad (20)$$

the electric current peaks in the central core as the magnetic field decreases abruptly with r . Within M2, it peaks as well at the jet boundary due to the poloidal magnetic field rapid vanishing (Chernoglazov et al. 2019).

To ensure the emitting particle number density does not exceed the total number density obtained within the MHD modelling, we set

$$k_e = n_{p,\gamma_{\min}}(r=0)(j'/\max(j'))^2. \quad (21)$$

The intensity profiles assuming Ohmic heating are presented in Figure 7. We see that due to the very narrow j' distribution, the central peaks are much more narrow than in case of the emission from the central dense core plasma in section 3. This narrow intensity peak, being smoothed by the convolution, provides the sufficiently lower intensity amplitude than in the previous models (compare Tables 4 and 6). The effect strengthens as the initial magnetization σ_M grows since in a highly magnetized jet the magnetic field derivatives are stronger across the jet, and the electric current density has even more narrow spatial distribution near the jet axis and at the very boundary.

In the case of high magnetization and considerable optical depth (≥ 20) the rapid j' growth at the jet boundary manifests itself in the intensity peak (the third column in the first row in Figure 7). Thus, the Ohmic heating can possibly account for the observed triple-peaked intensity profiles. Another very important consequence of such nonthermal particle distribution is the clear transverse symmetry that manifests in the brightening of both edges even for high bulk flow Lorentz factors.

4.3 Emitting plasma equipartition

Another possible emitting particle distribution discussed in Burbidge (1956); Blandford & Königl (1979) is the equipartition between the emitting particles energy and magnetic field in the plasma proper frame B' , which leads to $k_e \sim B'^2$. We do not expect suppression of the central core emission in this case. Indeed, the poloidal magnetic field B_p is almost constant within the central core (Beskin & Nokhrina 2009), while the toroidal component B_φ reaches the same amplitude at the light cylinder radius. Beyond R_L , both components fall with the conserved ratio $B_p/B_\varphi = R_L/r$ while plasma is relativistic (e.g., Lyubarsky 2009). For the strongly magnetized accelerating flow $\Gamma \approx r/R_L$, and both components are of the same order in the plasma proper frame (Lyutikov et al. 2005):

$$\frac{B'_p}{B'_\varphi} = \Gamma \frac{B_p}{B_\varphi} \approx 1. \quad (22)$$

Further along the jet for $r > \sigma_M R_L$, B'_φ dominates B'_p . However, in both cases the amplitude B'^2 is maximal within the core, and no emission suppression is expected: the central core dominates the optically thin jet. Indeed, we carried out the calculations with

$$k_e = \min\{B'^2/(8\pi mc^2), n_{p,\gamma_{\min}}\} \quad (23)$$

and did not get any noticeable difference between the equipartition regime and all the jet plasma emitting.

5 DISCUSSION

In Figure 8, we summarize the convolved intensity profiles at $\tau_{\max} = 1$ for the models with all jet plasma emitting according to a power-law distribution. The upper plot describes the viewing angle of 5° , and the lower plot describes the viewing angle of 15° . We chose $\tau_{\max} = 1$ to reflect the intensity behaviour close to radio core, though stratified models cannot be directly related to the Blandford-Königl model. The models with small d_{RL} values (low BH spins) and high initial magnetization σ_M provide the asymmetries, and no model demonstrates any distinguishable symmetric limb brightening. The best candidate for self-consistent limb brightening is the model with the total current closed inside a jet at high magnetization and high BH spin (see lower right part in Figure 3). In Figure 9, we additionally considered $\sigma_M = 200$ to demonstrate that the combination of higher magnetization and BH spin indeed results qualitatively in more symmetrical distinguishable limb brightening.

Regarding the magnetization and BH spin predictions, similarly to our work, Broderick & Loeb (2009) showed that low BH spins lead to strong asymmetries and high BH spins can produce limb brightening; Fuentes et al. (2018) showed triple-peaked intensity profiles in high magnetized jets. Helical magnetic fields in RMHD simulations by Kramer & MacDonald (2021) produced asymmetric intensity maps, while the magnetic fields in the models we considered also contain both poloidal and toroidal components.

Nevertheless, the profiles with qualitatively notable transverse structures are still optically thick and excessively bright. This questions the explanation of the multi-peaked intensity profiles solely by the high Lorentz-factors. The following reasoning also takes place. Within the Blandford-Königl (BK) model (Blandford & Königl 1979), the magnetic field and the amplitude of the particle number density at distance r are given by the relations

$$B(r) = B_0 \left(\frac{r_0}{r} \right), \quad (24)$$

$$k_e(r) = k_{e,0}(r) \left(\frac{r_0}{r} \right)^2. \quad (25)$$

These dependencies assume the homogeneity of the source and the equipartition between the magnetic and emitting particles energy densities. Though we consider the stratified models, we can compare their predictions with the observations using the BK model. We set 1 G and 10^3 cm^{-3} as fiducial values for the magnetic field and particle number density at 1 pc (e.g. Lobanov 1998). To compare, we average the magnetic field and emitting particle number density for our 15° models at $\tau_{\max} = 1$ and calculate the emitting particle number density predicted by BK model for such magnetic fields (last two lines in Tables 4, 5, 6). For all plasma emitting (Table 4), the means of the number density maxima, $\langle n'_{\max} \rangle$, and of the averaged per-model number densities, $\langle n'_{\text{average}} \rangle$, are two and one order of magnitude higher than predicted correspondingly. We keep in mind that the particle number density predicted in BK by the averaged magnetic field would be even lower. This suggests that not all the plasma in the jet emits. For 1 per cent of the emitting particles (Table 5), $\langle n'_{\max} \rangle$ is one order of magnitude higher than predicted by BK model, and $\langle n'_{\text{average}} \rangle$ has the same order of magnitude as predicted. So, the suppressed region of

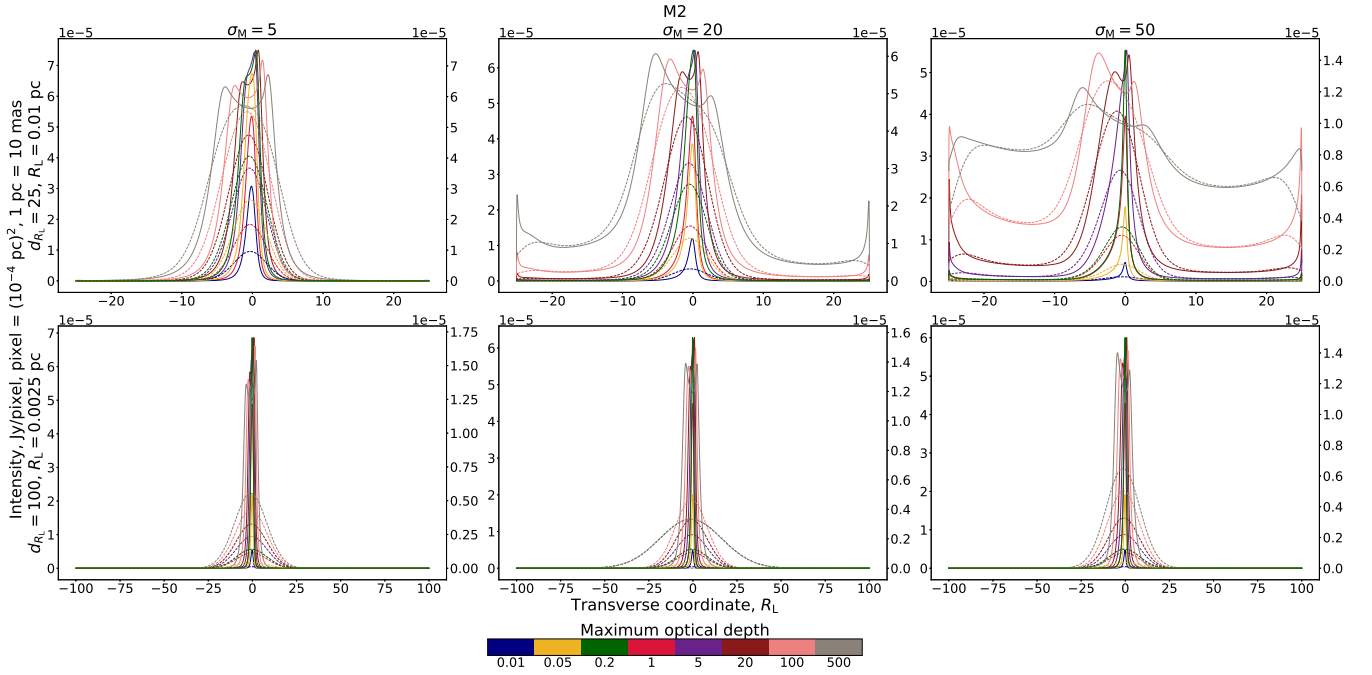


Figure 7. The ideal (solid lines) and convolved (dashed lines) intensity profiles in M2 at the viewing angle 15° for Ohmic heating ($k_e \sim j'^2$). The R_L values are chosen in the ‘ R_L comparison’ mode (the first and second row for each model describe the jet cross-section of the same geometrical width, 0.5 pc, but with a different light cylinder radii, see details in subsection 3.1). The colours correspond to the maximum optical depth over the cross-section, τ_{\max} . $\tau_{\max} \leq 1$ are plotted at the left y-axis, and $\tau_{\max} < 1$ are plotted at the right y-axis. The convolving beam is round with the FWHM equal to 0.1 of the cross-section width (0.5 mas). The physical parameters for this figure are summarized in Tables 6 and A4.

M	σ_M	d_{R_L}	Ψ_0 , 10^{34} G cm^2	W_{jet} , $10^{44} \text{ erg s}^{-1}$	n'_{\max} , cm^{-3}	n'_{average} , cm^{-3}	B'_{\max} , G	B'_{average} , G	I_{\max} , $\mu\text{Jy/pixel}$
M2	5	25	1.33	0.70	2048	65	0.112	0.032	18.33
M2	20	25	4.49	8.03	1708	37	0.150	0.053	15.46
M2	50	25	9.86	38.78	2016	21	0.209	0.085	11.07
M2	5	100	0.17	0.19	5054	45	0.134	0.013	4.61
M2	20	100	0.62	2.46	4029	31	0.160	0.020	4.27
M2	50	100	1.36	11.81	3715	26	0.175	0.026	4.04
average					3100	38	0.157		
BK					25		0.157		

Table 6. The physical parameters for the maximum optical depth of $\tau_{\max} = 1$ in Figure 7. The last but one line presents the averaged over the models magnetic field and particle number density, and the last line presents the Blandford-Königl model prediction of particle number density for such magnetic field (see section 5).

the jet should indeed occupy almost whole cross-section. For Ohmic heating (Table 6), $\langle n'_{\max} \rangle$ is very high as the proper electric current tends to delta-like behaviour at high magnetization and BH spin subsection 4.2, so $\langle n'_{\text{average}} \rangle$ is more applicable for comparison. This value differs from the predicted by BK model by less than two times. Thus, among the all plasma emitting, 1 per cent emitting and Ohmic heating, Ohmic heating provides the best correspondence between equipartition-predicted and actual emitting plasma number density.

Regarding the intensity profiles, in Figure 10, we show the convolved intensity profiles at $\tau_{\max} = 1$ for the models with the suppressed central core. In the upper plot, only 1 per cent of central core plasma emits, and in the lower

plot it is only 0.1 per cent. The viewing angle is 15° . The profiles demonstrate that a qualitative triple-peaked structure indeed requires this degree of central core suppression. We note that the averaged optical depths for these $\tau_{\max} = 1$ sources have the order of 0.01. The limb-brightened intensity profiles obtained by Takahashi et al. (2018); Ogihara et al. (2019) also required the enforcing of the emitting plasma transverse stratification.

In Figure 11, we show the convolved intensity profiles for the high magnetized ($\sigma_M = 200$) models where the emitting plasma is distributed according to Ohmic heating. We did not choose the particular τ_{\max} value here, as the Ohmic heated region is extremely narrow. Particularly, at $\tau_{\max} = 500$ here, τ_{average} is just $\approx 6 \cdot 10^{-4}$, so such source

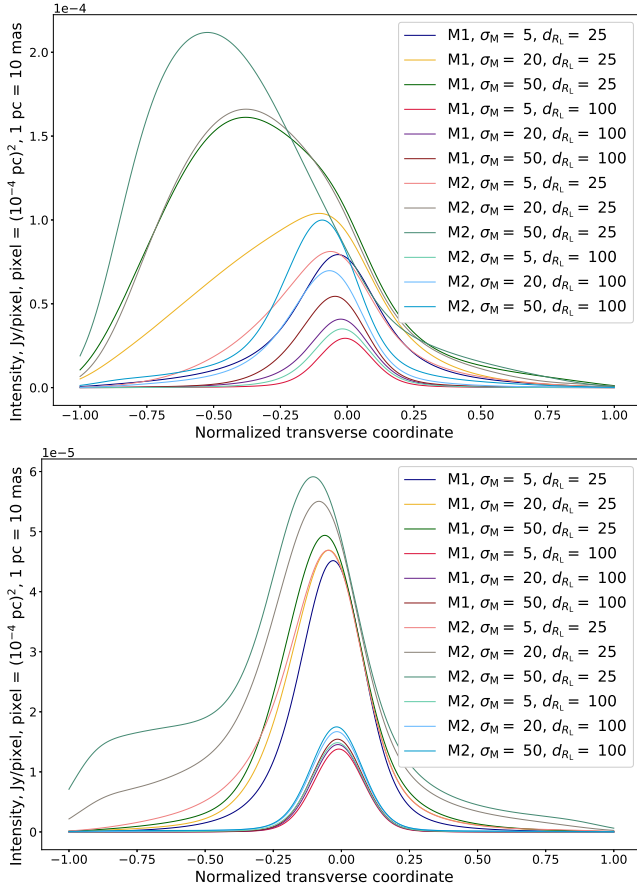


Figure 8. The convolved intensity profiles at $\tau_{\max} = 1$ for the models with all jet plasma emitting according to a power-law distribution. The viewing angles are 5° and 15° for upper and lower plots correspondingly.

is actually optically thin. The plot shows that Ohmic heating provides symmetric, limb-brightened profiles, and the net intensity profile is the most realistic among the cases considered in the paper.

Other derived parameters for the models are presented in the tables A1, A2, A3, A4, B1. In order not to overload the reader with similar data, we limited the tables to three distinctive τ_{\max} values: 0.01, 1, 100. Excluding few of the optically thick cases, we see that the total magnetic flux has the order of $10^{33} - 10^{34} \text{ G cm}^2$ and the jet power mostly has the order of $10^{43} - 10^{44} \text{ erg s}^{-1}$, with few cases of $10^{42} \text{ erg s}^{-1}$ for a weakly magnetized jets and of $10^{45} \text{ erg s}^{-1}$ for a strongly magnetized jets.

Thus, we conclude that likely not all of jet plasma is involved in the radiation, though the mechanism should be investigated further. In Frolova et al. in prep., we are deriving the particular fitting parameters for radio galaxy M87 and quasar 3C 273.

6 SUMMARY AND RESULTS

Recent VLBI observations have revealed the AGNs with multi-peaked transverse intensity profiles, among them Mrk501 (Giroletti et al. 2004), M87 (Hada 2017; Walker et al. 2018), 3C 84 (Giovannini et al. 2018), Cen A

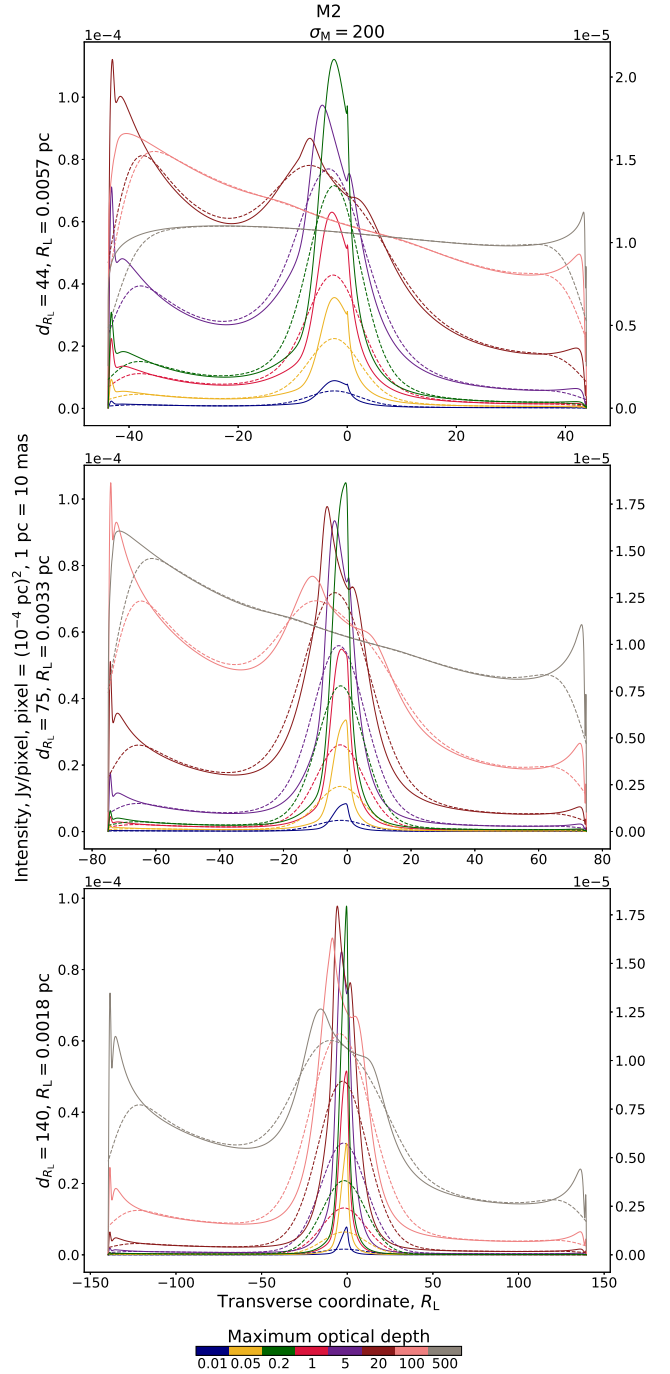


Figure 9. The intensity profiles for the magnetization $\sigma_M = 200$ in the M2 with all jet plasma emitting according to a power-law distribution. The ideal intensity profiles are plotted in solid lines, and the convolved intensity profiles are plotted in dashed lines. The viewing angle is 15° . The values of $\tau_{\max} < 1$ are plotted in the right y-axis.

(Janssen et al. 2021), 3C 273 (Bruni et al. 2021). In this paper, we investigate the possible origins of such intensity profiles by calculating self-absorbed synchrotron emission from the stratified jets. The jet structure is obtained within semi-analytical magnetohydrodynamical models with a constant angular velocity (M1, Beskin & Nokhrina (2006); Lyubarsky

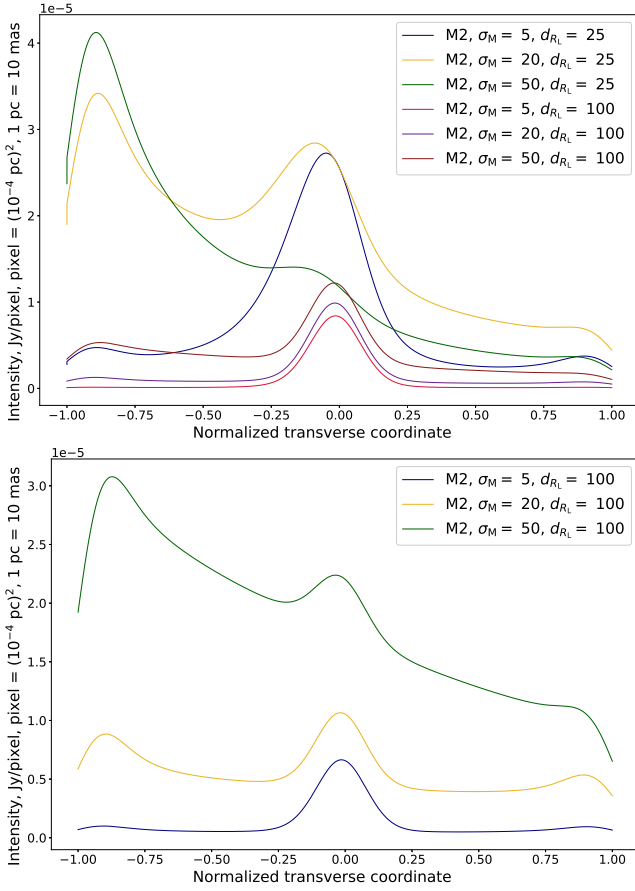


Figure 10. The convolved intensity profiles at $\tau_{\max} = 1$ for the models with the suppressed central core. In the upper plot, only 1 per cent of central core plasma emits, and in the lower plot it is only 0.1 per cent. The viewing angle is 15° .

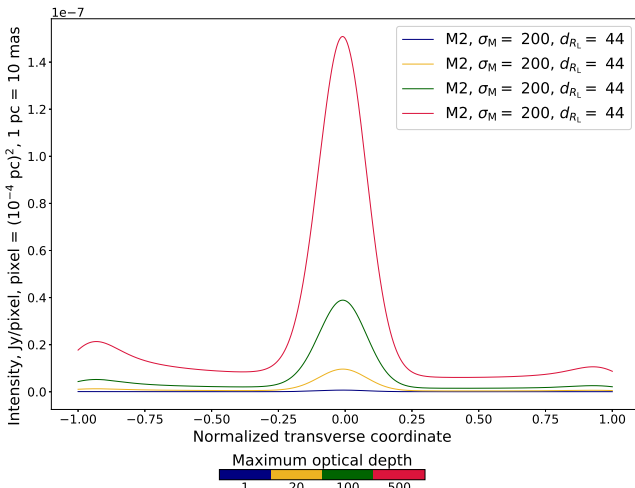


Figure 11. The convolved intensity profiles in the high magnetized ($\sigma_M = 200$) models where the emitting plasma is distributed according to Ohmic heating. The viewing angle is 15° .

(2009)) and with the current closed inside the jet (M2, Beskin et al. (2017); Kovalev et al. (2020)).

We obtained the following results. If we assume that all the particles in a jet, obtained within the MHD models, emit, then the jet emission must be dominated by the dense central part of the jet – the central core. Its existence has been predicted in both analytical (Beskin & Nokhrina 2009) and numerical models (Komissarov et al. 2009), thus, it is a robust result of MHD modelling. For most of the model parameters the central core results in spine-brightened profiles with weak and asymmetrical edge effects, if present. However, the total spectral flux in this case exceeds the typical observed value by several orders of magnitude. Thus, we conclude, that if the nonthermal particles spatial distribution is proportional to the total particle number density, then only a small fraction of all plasma emits. This is in agreement with the models of particle acceleration on shocks or in reconnection events (Sironi & Spitkovsky 2011; Sironi et al. 2013; Sironi & Spitkovsky 2014).

For such spatial distribution of the nonthermal particles, the double-peaked intensity profile appears in optically thick jets, transiting into one-peak profile for more optically thin regime. It can qualitatively explain the spine-to-limb brightening transition at $1.6 - 4.8$ GHz in 3C 273 observed by Bruni et al. (2021).

For a jets with large initial magnetization (and large bulk flow Lorentz factor), we observe the shift of intensity peak to the receding part of a jet. In this case we predict that multifrequency polarimetric observations must yield the Faraday rotation map with only one sign, as is observed by Gabuzda et al. (2017); Gabuzda (2021). As we move along a jet, the peak shifts closer to the jet axis. This may lead to an apparent change in the jet position angle even for a intrinsically straight jets.

We observe that in stratified jets, the limb brightening cannot be solely attributed to the presence of a slow flow at the jet boundary. Although the de-boosting of the edge emission provides some increase to the observed intensity, the overall decrease of the particle number density and magnetic field suppresses it. In order to explain the sufficient brightening of the jet edges, one needs low velocity, high particle number density and high magnetic field. If the first two conditions can be fulfilled considering the disk wind, obtaining the necessary high magnetic field may be problematic. Thus, we conclude, that spatial nonthermal particle distribution cannot explain the observed jet emission features.

We explore different spatial distributions of nonthermal particles. We find that the model with distribution (21), suggested by Lyutikov et al. (2005), is a promising one: i. it provides the values of a spectral flux at the observed levels; ii. the model with a total electric current closed inside a jet yields the triple-peaked intensity profile; iii. the intensity distribution is symmetrical. On the other hand, a model with the emitting particle number density proportional to the magnetic energy density in the plasma proper frame results in a strong central core dominance. Thus, this model is unlikely.

We also consider the following emitting particles spatial distribution: up to some radius some fixed fraction of all particles radiate. This suppresses the central core emission, while leaving such interesting features as a change in a jet position angle and one sign of Faraday Rotation Measure.

Outward from this radius all the plasma emits. This allows us to explain the triple-peaked intensity profile and the transition from triple-peaked to single-peaked profiles down the jet. Such spatial distribution can be advocated by the following two reasons. First, if the formation of the nonthermal relativistic plasma distribution is due to the magnetic field dissipation (for example, reconnection), then the plasma in a central core would remain non-relativistic and non-emitting, as it dominates the magnetic field in this region. Second, the particles acceleration may be due to reconnection events as a result of instabilities, and such events are expected near the jet boundary. In this case the nonthermal emitting particles appear mainly at the jet edges.

We conclude that the modelling of the observed intensity profiles in the resolved nearby jets by self-absorbed synchrotron emission from the stratified jets constrains the spatial distribution of the emitting plasma. We suggest that the models described in [subsection 4.1](#) and [subsection 4.2](#) are the preferred ones. In the first case the particles must be accelerated with the formation of a power-law energy distribution mainly at the jet edges due to the interaction with the collimating medium (e.g. instabilities triggering the magnetic reconnection). In the second case, the spatial distribution of the emitting particles forms due to Ohmic heating. The future work on the quantitative reproduction of intensity profiles observed in M87 by [Asada et al. \(2016\)](#) and [Nikonov et al. submitted](#) and in 3C 273 ([Bruni et al. 2021](#)) together with the polarization images modelling will allow us to further constrain the possible mechanisms of plasma heating.

ACKNOWLEDGEMENTS

We thank the referee, Joana Kramer, for helpful comments and suggestions that significantly improved the manuscript. This study has been supported by the Russian Science Foundation: project² 20-72-10078. This research made use of the data from the MOJAVE database³ which is maintained by the MOJAVE team ([Lister et al. 2018](#)). This research made use of NASA’s Astrophysics Data System.

DATA AVAILABILITY

The data underlying this research will be shared on reasonable request to the corresponding author.

REFERENCES

- Araudo A. T., Bosch-Ramon V., Romero G. E., 2011, in ed., *Jets at all Scales, Proceedings of the International Astronomical Union, IAU Symposium, Volume 275*. pp 131–135
- Asada K., Nakamura M., Pu H.-Y., 2016, *ApJ*, **833**, 56
- Ball D., Sironi L., Özel F., 2018, *ApJ*, **862**, 80
- Beskin V. S., 2010, *Physics Uspekhi*, **53**, 1199
- Beskin V. S., Malyshev L. M., 2000, *Astronomy Letters*, **26**, 208
- Beskin V. S., Nokhrina E. E., 2006, *MNRAS*, **367**, 375
- Beskin V. S., Nokhrina E. E., 2009, *MNRAS*, **397**, 1486
- Beskin V., Chernoglazov A., Kiselev A., Nokhrina E., 2017, *MNRAS*, **472**, 3971
- Biretta J. A., Sparks W. B., Macchetto F., 1999, *ApJ*, **520**, 621
- Blandford R. D., Königl A., 1979, *ApJ*, **232**, 34
- Blandford R. D., Payne D. G., 1982, *MNRAS*, **199**, 883
- Blandford R., Znajek R., 1977, *MNRAS*, **179**, 433
- Blandford R., Meier D., Readhead A., 2019, *Annual Review of Astronomy and Astrophysics*, **57**, 467
- Broderick A. E., Loeb A., 2009, *ApJ*, **697**, 1164
- Bromberg O., Tchekhovskoy A., 2016, *MNRAS*, **456**, 1739
- Bruni G., et al., 2021, arXiv e-prints, p. [arXiv:2101.07324](#)
- Burbidge G., 1956, *ApJ*, **124**, 416
- Chatterjee K., Liska M., Tchekhovskoy A., Markoff S. B., 2019, *MNRAS*, **490**, 2200
- Chernoglazov A. V., Beskin V. S., Pariev V. I., 2019, *MNRAS*, **488**, 224
- Cruz-Orsio A., et al., 2022, *Nature Astronomy*, **6**, 103
- Event Horizon Telescope Collaboration et al., 2019a, *ApJ*, **875**, L1
- Event Horizon Telescope Collaboration et al., 2019b, *ApJ*, **875**, L5
- Fromm C. M., et al., 2022, *A&A*, **660**, A107
- Fuentes A., Gómez J. L., Martí J. M., Perucho M., 2018, *ApJ*, **860**, 121
- Gabuzda D., 2021, *Galaxies*, **9**, 58
- Gabuzda D. C., Roche N., Kirwan A., Knuettel S., Nagle M., Houston C., 2017, *MNRAS*, **472**, 1792
- Ginzburg V. L., Syrovatskii S. I., 1965, *ARA&A*, **3**, 297
- Giovannini G., et al., 2018, *Nature Astronomy*, **2**, 472
- Giroletti M., et al., 2004, *ApJ*, **600**, 127
- Hada K., 2017, *Galaxies*, **5**, 2
- Hardee P. E., Eilek J. A., 2011, *ApJ*, **735**, 61
- Hirofani K., 2005, *ApJ*, **619**, 73
- Homan D. C., et al., 2021, *ApJ*, **923**, 67
- Hovatta T., et al., 2014, *AJ*, **147**, 143
- Janssen M., Falcke H., Kadler M., Ros E., Wielgus M., et al. 2021, *Nature Astronomy*, **5**, 1017
- Kim J. Y., et al., 2018, *A&A*, **616**, A188
- Kino M., Takahashi M., Kawashima T., Park J., Hada K., Ro H., Cui Y., 2022, *ApJ*, **939**, 83
- Kirk J., Melrose D., Priest E., Benz A., Courvoisier T.-L., 1994, in *Saas-Fee Advanced Course 24: Plasma Astrophysics*.
- Komissarov S. S., Barkov M. V., Vlahakis N., Königl A., 2007, *MNRAS*, **380**, 51
- Komissarov S. S., Vlahakis N., Königl A., Barkov M. V., 2009, *MNRAS*, **394**, 1182
- Kovalev Y., Lobanov A., Pushkarev A., Zensus J., 2008, *Astronomy & Astrophysics*, **483**, 759
- Kovalev Y., Pushkarev A., Nokhrina E., Plavin A., Beskin V., Chernoglazov A., Lister M., Savolainen T., 2020, *MNRAS*, **495**, 3576
- Kramer J. A., MacDonald N. R., 2021, *A&A*, **656**, A143
- Kutkin A. M., Pashchenko I. N., Sokolovsky K. V., Kovalev Y. Y., Aller M. F., Aller H. D., 2019, *MNRAS*, **486**, 430
- Levinson A., Globus N., 2017, *MNRAS*, **465**, 1608
- Lister M. L., Aller M. F., Aller H. D., Hodge M. A., Homan D. C., Kovalev Y. Y., Pushkarev A. B., Savolainen T., 2018, *ApJS*, **234**, 12
- Lister M. L., et al., 2019, *ApJ*, **874**, 43
- Lobanov A. P., 1998, *A&A*, **330**, 79
- Lu R.-S., et al., 2023, *Nature*, **616**, 686–690
- Lyubarsky Y., 2009, *ApJ*, **698**, 1570
- Lyutikov M., Pariev V. I., Gabuzda D. C., 2005, *MNRAS*, **360**, 869
- McKinney J. C., 2006, *MNRAS*, **368**, 1561
- Mertens F., Lobanov A. P., Walker R. C., Hardee P. E., 2016, *A&A*, **595**, A54
- Mościbrodzka M., Falcke H., Shiokawa H., 2016, *A&A*, **586**, A38
- Nakamura M., Meier D. L., 2014, *ApJ*, **785**, 152

² Information about the project:

<https://rscf.ru/en/project/20-72-10078/>

³ <https://www.cv.nrao.edu/MOJAVE/>

- Nakamura M., Asada K., Hada K., et al. 2018, [ApJ](#), **898**, 146
- Nokhrina E., 2017, [MNRAS](#), **468**, 2372
- Nokhrina E., 2018, in K. Asada, E. de Gouveia dal Pino, H. Nagai, R. Nemmen, M. Giroletti ed., *Perseus in Sicily: from black hole to cluster outskirts*, Proceedings IAU Symposium No. 342.
- Nokhrina E. E., Beskin V. S., Kovalev Y. Y., Zheltoukhov A. A., 2015, [MNRAS](#), **447**, 2726
- Nokhrina E. E., Gurvits L. I., Beskin V. S., Nakamura M., Asada K., Hada K., 2019, [MNRAS](#), **489**, 1197
- Nokhrina E. E., Kovalev Y. Y., Pushkarev A. B., 2020, [MNRAS](#), **498**, 2532
- Nokhrina E. E., Pashchenko I. N., Kutkin A. M., 2022, [MNRAS](#), **509**, 1899
- O’Sullivan S. P., Gabuzda D. C., 2009, [MNRAS](#), **400**, 26
- Ogihara T., Takahashi K., Toma K., 2019, [ApJ](#), **877**, 19
- Ostrowski M., 1990, [A&A](#), **238**, 435
- Ostrowski M., 1998, [A&A](#), **335**, 134
- Pashchenko I. N., Kravchenko E. V., Nokhrina E. E., Nikonov A. S., 2023, [arXiv e-prints](#), p. [arXiv:2301.12861](#)
- Plavin A. V., Kovalev Y. Y., Pushkarev A. B., Lobanov A. P., 2019, [MNRAS](#), **485**, 1822
- Pushkarev A. B., Kovalev Y. Y., 2012, [A&A](#), **544**, A34
- Pushkarev A. B., Hovatta T., Kovalev Y. Y., Lister M. L., Lobanov A. P., Savolainen T., Zensus J. A., 2012, [A&A](#), **545**, A113
- Pushkarev A. B., Kovalev Y. Y., Lister M. L., Savolainen T., 2017, [MNRAS](#), **468**, 4992
- Rybicki G. B., Lightman A. P., 1979, *Radiative processes in astrophysics*. WILEY
- Sironi L., Spitkovsky A., 2011, [ApJ](#), **726**, 75
- Sironi L., Spitkovsky A., 2014, [ApJ](#), **783**, L21
- Sironi L., Spitkovsky A., Arons J., 2013, [ApJ](#), **771**, 54
- Stone J. M., Pringle J. E., Begelman M. C., 1999, [MNRAS](#), **310**, 1002
- Takahashi K., Toma K., Kino M., Nakamura M., Hada K., 2018, [ApJ](#), **868**, 82
- Tchekhovskoy A., McKinney J. C., Narayan R., 2009, [ApJ](#), **699**, 1789
- Vaidya B., Mignone A., Bodo G., Rossi P., Massaglia S., 2018, [ApJ](#), **865**, 144
- Walker R. C., Hardee P. E., Davies F. B., Ly C., Junor W., 2018, [ApJ](#), **855**, 128
- Wardle J. F. C., Homan D. C., Ojha R., Roberts D. H., 1998, [Nature](#), **395**, 457
- Zakamska N. L., Begelman M. C., Blandford R. D., 2008, [ApJ](#), **679**, 990
- Zamaninasab M., Clausen-Brown E., Savolainen T., Tchekhovskoy A., 2014, [Nature](#), **510**, 126
- Zdziarski A. A., Egron E., 2022, [The Astrophysical Journal Letters](#), **935**, L4
- Zdziarski A. A., Phuravathu D. G., Sikora M., Böttcher M., Chibueze J. O., 2022, [The Astrophysical Journal Letters](#), **928**, L9

This paper has been typeset from a \LaTeX file prepared by the author.

APPENDIX A: THE OPTICALLY THIN AND THICK PHYSICAL PARAMETERS

We present the characteristic physical parameters in substantially optically thin ($\tau_{\text{max}} = 0.01$) and thick ($\tau_{\text{max}} = 100$) conditions for Figures 2 (Table A1), 3 (Table A2), 6 (Table A3), 7 (Table A4) and for Figure 5 representing the jet at different distances from the central engine (Table B1).

APPENDIX B: THE PHYSICAL PARAMETERS AT DIFFERENT DISTANCES FROM THE CENTRAL ENGINE

We present the characteristic physical parameters for the maximum optical depth of $\tau_{\text{max}} = 1$ and in substantially optically thin ($\tau_{\text{max}} = 0.01$) and thick ($\tau_{\text{max}} = 100$) conditions for Figure 5 representing the jet at different distances from the central engine (Table B1).

M	σ_M	d_{R_L}	τ_{\max}	$\Psi_0,$ 10^{34} G cm^2	$W_{\text{jet}},$ $10^{44} \text{ erg s}^{-1}$	$n'_{\max},$ cm^{-3}	$n'_{\text{average}},$ cm^{-3}	$B'_{\max},$ G	$B'_{\text{average}},$ G	$I_{\max},$ $\mu\text{Jy/pixel}$
M1	5	25	0.01	0.45	0.08	145	16	0.017	0.004	1.90
M1	5	25	100	4.47	7.98	14529	1557	0.173	0.044	216.00
M1	20	25	0.01	0.79	0.25	81	9	0.022	0.006	2.51
M1	20	25	100	7.94	25.15	8069	915	0.217	0.063	326.86
M1	50	25	0.01	1.35	0.72	60	7	0.024	0.008	3.83
M1	50	25	100	13.48	72.49	5995	713	0.237	0.079	323.53
M1	5	100	0.01	0.06	0.02	372	10	0.022	0.002	0.65
M1	5	100	100	0.56	2.03	37168	1024	0.219	0.019	163.44
M1	20	100	0.01	0.11	0.08	224	6	0.027	0.003	0.88
M1	20	100	100	1.10	7.67	22368	640	0.272	0.028	249.28
M1	50	100	0.01	0.20	0.27	181	5	0.029	0.003	1.17
M1	50	100	100	2.05	26.81	18063	537	0.294	0.034	293.00
M2	5	25	0.01	0.27	0.03	83	11	0.023	0.006	1.96
M2	5	25	100	2.67	2.84	8285	1095	0.225	0.063	174.45
M2	20	25	0.01	0.77	0.24	51	7	0.026	0.009	4.29
M2	20	25	100	7.73	23.84	5071	714	0.259	0.092	195.24
M2	50	25	0.01	1.15	0.53	28	4	0.025	0.010	5.79
M2	50	25	100	11.54	53.16	2763	404	0.245	0.099	177.24
M2	5	100	0.01	0.04	0.01	219	7	0.028	0.003	0.76
M2	5	100	100	0.36	0.81	21948	687	0.279	0.028	184.73
M2	20	100	0.01	0.12	0.09	153	5	0.031	0.004	1.50
M2	20	100	100	1.21	9.33	15300	499	0.312	0.039	323.09
M2	50	100	0.01	0.25	0.41	129	4	0.033	0.005	2.22
M2	50	100	100	2.53	40.95	12877	437	0.325	0.049	321.51

Table A1. The physical parameters in substantially optically thin ($\tau_{\max} = 0.01$) and thick ($\tau_{\max} = 100$) conditions in Figure 2.

M	σ_M	d_{R_L}	τ_{\max}	$\Psi_0,$ 10^{34} G cm^2	$W_{\text{jet}},$ $10^{44} \text{ erg s}^{-1}$	$n'_{\max},$ cm^{-3}	$n'_{\text{average}},$ cm^{-3}	$B'_{\max},$ G	$B'_{\text{average}},$ G	$I_{\max},$ $\mu\text{Jy/pixel}$
M1	5	25	0.01	0.56	0.13	228	24	0.022	0.005	1.07
M1	5	25	100	5.60	12.50	22755	2439	0.217	0.055	129.97
M1	20	25	0.01	1.02	0.41	132	15	0.028	0.008	1.11
M1	20	25	100	10.16	41.20	13217	1498	0.277	0.081	122.46
M1	50	25	0.01	1.77	1.24	103	12	0.031	0.010	1.18
M1	50	25	100	17.65	124.30	10279	1222	0.311	0.103	106.40
M1	5	100	0.01	0.07	0.03	578	16	0.027	0.002	0.31
M1	5	100	100	0.70	3.16	57810	1593	0.274	0.024	87.31
M1	20	100	0.01	0.16	0.15	449	13	0.039	0.004	0.32
M1	20	100	100	1.55	15.38	44851	1283	0.385	0.039	87.79
M1	50	100	0.01	0.26	0.44	293	9	0.037	0.004	0.34
M1	50	100	100	2.61	43.55	29345	872	0.374	0.043	85.10
M2	5	25	0.01	0.33	0.04	130	17	0.028	0.008	1.11
M2	5	25	100	3.34	4.45	12976	1716	0.282	0.079	127.83
M2	20	25	0.01	1.00	0.40	85	12	0.034	0.012	1.33
M2	20	25	100	10.04	40.20	8549	1203	0.336	0.119	122.12
M2	50	25	0.01	1.82	1.32	68	10	0.039	0.016	1.48
M2	50	25	100	18.17	131.79	6849	1002	0.386	0.157	92.13
M2	5	100	0.01	0.04	0.01	344	11	0.035	0.003	0.33
M2	5	100	100	0.45	1.27	34438	1077	0.350	0.035	94.83
M2	20	100	0.01	0.16	0.15	252	8	0.040	0.005	0.37
M2	20	100	100	1.55	15.38	25235	823	0.401	0.050	88.54
M2	50	100	0.01	0.33	0.70	220	7	0.043	0.006	0.39
M2	50	100	100	3.31	70.02	22019	748	0.426	0.064	80.35

Table A2. The physical parameters in substantially optically thin ($\tau_{\max} = 0.01$) and thick ($\tau_{\max} = 100$) conditions in Figure 3.

M	σ_M	d_{R_L}	τ_{\max}	$\Psi_0,$ 10^{34} G cm^2	$W_{\text{jet}},$ $10^{44} \text{ erg s}^{-1}$	$n'_{\max},$ cm^{-3}	$n'_{\text{average}},$ cm^{-3}	$B'_{\max},$ G	$B'_{\text{average}},$ G	$I_{\max},$ $\mu\text{Jy/pixel}$
M2	5	25	0.01	1.05	0.44	151	7	0.089	0.025	0.65
M2	5	25	100	10.51	44.03	15070	674	0.887	0.250	60.52
M2	20	25	0.01	2.68	2.87	170	5	0.090	0.032	0.79
M2	20	25	100	26.84	287.46	16983	457	0.898	0.319	50.08
M2	50	25	0.01	3.18	4.04	92	2	0.068	0.027	0.96
M2	50	25	100	31.82	403.93	9191	188	0.676	0.274	60.89
M2	5	100	0.01	0.14	0.13	44	2	0.111	0.011	0.19
M2	5	100	100	1.41	12.69	4359	219	1.107	0.110	54.42
M2	20	100	0.01	0.49	1.54	91	2	0.127	0.016	0.22
M2	20	100	100	4.90	153.55	9147	207	1.266	0.159	59.13
M2	50	100	0.01	1.04	6.94	158	2	0.134	0.020	0.26
M2	50	100	100	10.43	694.06	15810	220	1.340	0.201	91.10

Table A3. The physical parameters in substantially optically thin ($\tau_{\max} = 0.01$) and thick ($\tau_{\max} = 100$) conditions in Figure 6.

M	σ_M	d_{R_L}	τ_{\max}	$\Psi_0,$ 10^{34} G cm^2	$W_{\text{jet}},$ $10^{44} \text{ erg s}^{-1}$	$n'_{\max},$ cm^{-3}	$n'_{\text{average}},$ cm^{-3}	$B'_{\max},$ G	$B'_{\text{average}},$ G	$I_{\max},$ $\mu\text{Jy/pixel}$
M2	5	25	0.01	0.42	0.07	205	6	0.035	0.010	9.58
M2	5	25	100	4.19	7.02	20480	646	0.354	0.100	54.94
M2	20	25	0.01	1.42	0.80	171	4	0.047	0.017	3.20
M2	20	25	100	14.19	80.32	17083	370	0.475	0.169	54.47
M2	50	25	0.01	3.12	3.88	202	2	0.066	0.027	0.26
M2	50	25	100	31.18	387.80	20156	213	0.662	0.269	48.02
M2	5	100	0.01	0.05	0.02	505	4	0.042	0.004	0.11
M2	5	100	100	0.54	1.86	50540	445	0.424	0.042	17.48
M2	20	100	0.01	0.20	0.25	403	3	0.051	0.006	0.10
M2	20	100	100	1.96	24.55	40286	313	0.506	0.064	18.72
M2	50	100	0.01	0.43	1.18	372	3	0.055	0.008	0.10
M2	50	100	100	4.30	118.15	37155	264	0.553	0.083	20.11

Table A4. The physical parameters in substantially optically thin ($\tau_{\max} = 0.01$) and thick ($\tau_{\max} = 100$) conditions in Figure 7.

M	σ_M	d_{R_L}	τ_{\max}	$\Psi_0,$ 10^{34} G cm^2	$W_{\text{jet}},$ $10^{44} \text{ erg s}^{-1}$	$n'_{\max},$ cm^{-3}	$n'_{\text{average}},$ cm^{-3}	$B'_{\max},$ G	$B'_{\text{average}},$ G	$I_{\max},$ $\mu\text{Jy/pixel}$
M1	5	50	0.01	0.45	0.08	112	6	0.013	0.002	0.94
M1	5	50	1	1.41	0.80	1120	61	0.042	0.006	46.00
M1	5	50	100	4.47	7.98	11196	612	0.133	0.020	194.21
M1	5	100	0.01	0.45	0.08	91	3	0.011	0.001	0.54
M1	5	100	1	1.41	0.80	912	25	0.034	0.003	28.35
M1	5	100	100	4.47	7.98	9119	251	0.109	0.010	177.07
M1	50	50	0.01	1.35	0.72	40	2	0.016	0.003	0.89
M1	50	50	1	4.26	7.25	402	24	0.050	0.010	45.66
M1	50	50	100	13.48	72.49	4017	239	0.159	0.032	357.26
M1	50	100	0.01	1.35	0.72	31	1	0.012	0.001	0.36
M1	50	100	1	4.26	7.25	305	9	0.038	0.004	19.53
M1	50	100	100	13.48	72.49	3052	91	0.121	0.014	259.04
M2	50	50	0.01	1.15	0.53	15	1	0.013	0.004	0.71
M2	50	50	1	3.65	5.32	151	11	0.042	0.011	38.44
M2	50	50	100	11.54	53.16	1513	109	0.134	0.035	374.31
M2	50	100	0.01	1.15	0.53	10	0	0.009	0.001	0.14
M2	50	100	1	3.65	5.32	104	4	0.029	0.004	7.87
M2	50	100	100	11.54	53.16	1045	35	0.093	0.014	245.54
M1	50	50	0.01	1.77	1.24	69	4	0.021	0.004	0.39
M1	50	50	1	5.58	12.43	689	41	0.066	0.013	19.83
M1	50	50	100	17.65	124.30	6888	410	0.208	0.041	115.86
M1	50	100	0.01	1.77	1.24	52	2	0.016	0.002	0.18
M1	50	100	1	5.58	12.43	523	16	0.050	0.006	9.83
M1	50	100	100	17.65	124.30	5234	156	0.158	0.018	107.68
M2	50	50	0.01	1.82	1.32	38	3	0.021	0.006	0.27
M2	50	50	1	5.75	13.18	375	27	0.067	0.018	14.36
M2	50	50	100	18.17	131.79	3751	270	0.211	0.055	109.39
M2	50	100	0.01	1.82	1.32	26	1	0.015	0.002	0.09
M2	50	100	1	5.75	13.18	259	9	0.046	0.007	5.15
M2	50	100	100	18.17	131.79	2590	88	0.146	0.022	96.31

Table B1. The parameters for Figure 5 (see also Tables 3, 4, A1, A2).